Double Asteroid Redirection Test (DART): Structural and dynamic interactions between asteroidal elements of Binary Asteroid (65803) Didymos

Masatoshi Hirabayashi,[1] Fabio Ferrari,[2] Martin Jutzi,[2] Ryota Nakano,[1] Sabina D. Raducan,[2] Paul Sánchez,[3] Stefania Soldini,[4] Yun Zhang,[5,6] Olivier S. Barnouin,[7] and Derek C. Richardson[8]

[1]*Department of Aerospace Engineering*
Auburn University
Auburn, AL, USA
[2]*Space Research and Planetary Sciences, Physics Institute*
University of Bern
Bern, Switzerland
[3]*Colorado Center for Astrodynamics Research*
University of Colorado Boulder
3775 Discovery Dr, Boulder, CO, USA
[4]*Department of Mechanical, Materials and Aerospace Engineering*
University of Liverpool
Liverpool, United Kingdom
[5]*Université Côte d'Azur*
Observatoire de la Côte d'Azur
CNRS, Laboratoire Lagrange, Nice, France
[6]*Department of Aerospace Engineering*
University of Maryland
College Park, MD, USA
[7]*Johns Hopkins University/Applied Physics Laboratory, Laurel, MD, USA*
[8]*Department of Astronomy*
University of Maryland
College Park, MD, USA

ABSTRACT

NASA's Double Asteroid Redirection Test (DART) mission is the first full-scale planetary defense mission. The target is the binary asteroid (65803) Didymos, in which the smaller component Dimorphos (∼164 m equivalent diameter) is orbiting the larger component Didymos (∼780 m equivalent diameter). The DART spacecraft hits Dimorphos, changing its orbital motion relative to Didymos, the magnitude of which directly correlates with DART's kinetic deflection capability. The spacecraft collision with Dimorphos creates an impact crater, contributing to this asteroid's reshaping process. Furthermore, collisions of ejected particles from the DART impact site on Dimorphos with Didymos, which may be close to structural failure due to its spin period, 2.26 h, may induce reshaping processes on Didymos if the delivered kinetic energy is high enough to fluidize materials. Here, we discuss recent findings of the Didymos-Dimorphos system's possible reshaping processes and the resulting interactions between structure and dynamics. While large uncertainties exist, potential reshaping scenarios may happen to Didymos and Dimorphos if the structural configurations meet such conditions. A statistical analysis reveals that, given a surface slope uncertainty of 45°, fast ejecta ($\gtrsim$14 m/s) may hit Didymos after the DART impact with 13% of chance, while slow ejecta within the initial ejecta cone (∼0.8 m/s) but traveling faster than the escape speed (∼0.43 m/s) may hit the asteroid with 8% of chance. Depending on the reshaping magnitude, the orbital perturbation is no longer negligible. If it happens, earth-based telescopic observations may detect such orbital evolution.

Corresponding author: Masatoshi Hirabayashi
thirabayashi@auburn.edu

1. INTRODUCTION

The NASA Direct Asteroid Redirection Test (DART) mission is the first planetary defense mission to test a kinetic impact deflection technology to redirect an asteroid effectively (e.g., Cheng et al. 2018; Rivkin et al. 2021). DART aims to make its spacecraft collide with Dimorphos, the smaller satellite of the S-type binary asteroid (65803) Didymos. For clarity, this paper later denotes this binary asteroid as the Didymos-Dimorphos system while calling Didymos the larger primary and Dimorphos the smaller secondary. The spacecraft was successfully launched on November 23, 2021, and the collision with Dimorphos is planned to happen on September 26, 2022. DART's almost face-to-face collision adds a kinetic momentum to Dimorphos, causing it to decelerate and have a shorter semi-major axis and thus a shorter mutual orbit period (Cheng et al. 2016, 2018). This impact event will be observed by LICIACube [ref] and ground- and spaced-based telescopes [ref]. Four years after the DART impact, ESA's Hera will visit the Didymos-Dimorphos system to detail explore its geologic origin and further advance planetary defense technologies [ref].

The nominal orbital change driven by the DART impact is ~ 73 sec, though many factors likely change the outcome (Rivkin et al. 2021). Quantifying the DART deflection capability applies a momentum transfer coefficient, β, i.e., a ratio of the actual momentum transfer to the ideal momentum transfer with no ejection (i.e., a completely inelastic collision) (e.g., Holsapple & Housen 2012; Cheng et al. 2016, 2018). The actual momentum transfer becomes higher than the ideal one if impact-driven ejecta depart from the impact site opposite the spacecraft direction. However, if a shock wave reaches the other side of the impact site, ejecta may leave along the spacecraft incoming direction, leading to a smaller β value, though this case is unlikely or almost negligible.

The baseline β assessment considers the mutual orbit under the assumption that Didymos and Dimorphos are structurally rigid; in other words, these bodies do not experience any reshaping while dynamically interacting with each other (Cheng et al. 2018). However, recent work suggests that coupling dynamics and structure may affect the momentum transfer if reshaping happens to these bodies (Hirabayashi et al. 2017, 2019a). Multiple factors may control Didymos' reshaping process on various scales (Zhang et al. 2017, 2021). The reshaping event then changes the mutual gravitational field, causing additional dynamic perturbation in the Didymos-Dimorphos system. If the reshaping process is large enough to cause an orbital period change greater than the measurement threshold (the DART Level-1 requirement), which is 7.3 s (Rivkin et al. 2021), better quantifying the β value requires appropriate assessments of how such a process affects the mutual dynamics after the DART impact.

Reshaping processes depend on how each body experiences the DART impact. Dimorphos undergoes a cratering process driven by the DART impact (Stickle et al. 2017, 2020; Rainey et al. 2020; et al. 2022b). While Rainey et al. (2020) suggested a rough estimate of DART impact-driven crater size as ~ 2 m diameter for a high-strength case and ~ 20 m diameter for a low-strength case, the crater formation strongly depends on the impact conditions and the surface and subsurface strengths (Raducan & Jutzi 2022). This process results in a permanent shape change. On the other hand, Didymos is currently rotating at a spin period of 2.26 h (Pravec et al. 2006), and its bulk density is 2170 ± 350 kg/m^3 (Naidu et al. 2020). Because of these conditions, the surface slope reaches 90° at latitudes lower than 45 deg (Naidu et al. 2020), inferring tension in the internal structure. If the internal structure is mechanically homogeneous, the body needs cohesive strength to resist structural failure (Naidu et al. 2020; Zhang et al. 2017, 2021). A mechanically strong interior, given cohesion, may allow surface layers to be strengthless, under which centrifugal and gravitational forces do not initiate material movements (Ferrari & Tanga 2022). After the DART impact, ejecta particles depart from the impact site and experience complex dynamics (Yu et al. 2017; Yu & Michel 2018; et al. 2022a). Some ejecta particles then fall onto Didymos with various impact speeds, depending on how the ejecta cone evolves (Yu et al. 2017; Yu & Michel 2018). If Didymos receives enough net kinetic energy to cause surface disturbances, material flows may occur, causing reshaping (Hirabayashi et al. 2017)

The primary issue is that because these bodies' physical properties are largely unknown, there is a limited clue on whether measurable reshaping processes do not occur to both of them. Therefore, analyses in general need a wide range of parametric assessment to quantify the system's response to the DART impact, challenging rigorous predictions about the reshaping processes. Such uncertainties define the following primary question:

- If measurable reshaping occurs to either Didymos or Dimorphos, how does the resulting orbital perturbation influence the β value?

This question further broadens the area of investigation to identify the following four questions, all of which are within the DART-4B category (Rivkin et al. 2021).

- What physical properties control reshaping on Didymos and Dimorphos?

Table 1: Major physical parameters used for discussions. For Dimensions, M is mass, L is length, and S is time.

Notation	Description	Dimensions
ρ_B	Bulk density	M/L^3
ρ_G	Grain density	M/L^3
T_{sp}	Didymos spin period	S
dT_{sp}	Didymos spin period change	S
dD	Didymos short axis length change	L
ω_{sp}	Didymos spin rate	$1/S$
U_g	Didymos gravity potential	L^2/S^2
(x, y, z)	Didymos body fixed frame	L
(ξ, η, ζ)	Dimorphos body fixed frame	L
dL	Dimorphos short axis length change	L
θ	Angle of internal friction	[-]
C_0	Bulk cohesive strength	M/LS^2
C_{crit}	Critical cohesive strength	M/LS^2
c	Interparticle cohesive strength	M/LS^2
V_x	Particle speed in the surface horizontal direction	L/S^2
V_D	DART impact speed	L/S^2
V_{ejc}	Collision speed of DART-driven ejecta on Didymos	L/S^2
M_D	DART spacecraft mass	M
M_{ejc}	DART-driven ejecta particle mass	M
P_{cr}	Crushing pressure	M/LS^2
ϕ_0	Initial bulk porosity	[-]
ψ_c	Volumetric ratio of strong core to entire body in Didymos	[-]
M_e	Mass ratio of ejected mass to total mass in Didymos	[-]

- If measurable reshaping occurs due to the DART impact, how does the Didymos-Dimorphos system structurally and dynamically respond?

- If the DART impact does not induce measurable reshaping, how does the current structure keep remaining intact during the impact event?

- How do the outcomes (both reshaping and non-reshaping) give insights into a binary asteroid' natural dynamical and structural evolution?

As part of the pre-impact reports from the DART investigation team, we summarize the current efforts to better understand the potential interactions between dynamics and structure after the DART impact. It is aligned with the efforts in the Dynamics Working group (Richardson et al. 2022) under joint collaborations with other working groups (et al. 2022b,a; **?**). The major purpose of this paper is to review the current understandings of multi-physics regimes (impact, dynamics, and structure) and visualize the questions regarding the interactions between dynamics and structure driven by the DART impact. This paper organizes two major sections. Section 2 introduces multiple team efforts related to the reshaping processes on Dimorphos and Didymos. This section also offers how to measure Didymos' reshaping magnitude. Section 3 focuses on orbital perturbation driven by reshaping of either Dimorphos or Didymos. The investigations in this section provide how the orbital period change correlates with the reshaping magnitude. Section 4 introduces interpretations of the analyses above. Unless there are explicitly stated definitions, the following discussions use parameters defined in Table 1 in the main discussions, while the appendix also uses additional parameters defined in Table 2.

2. RESHAPING MECHANISMS AND PROCESSES

2.1. *Impact-driven reshaping on Dimorphos*

The crater formation by the DART impact may strongly depend on physical parameters of both impactor and target conditions (e.g., Stickle et al. 2017; Rainey et al. 2020; Raducan et al. 2019; Raducan et al. 2020). Among the recent

efforts in characterizing the DART impact are numerical simulations using the Smoothed Particle Hydrodynamics (SPH) impact code (Jutzi et al. 2008; Jutzi 2015). They describe vertical and oblique DART-like impact scenarios on spherical and elliptical asteroid targets (Raducan & Jutzi 2022), where the impactor mass, M_D, and the impact speed, V_D, are approximately 500 kg and 6 km/sec, respectively. Throughout the simulations, the pressure-dependent strength model (Collins et al. 2004) defines the material strength, given the cohesive strength, C_0, and the angle of internal friction, θ, as free parameters. The initial target porosity, ϕ_0, is 40% based on the $P - \alpha$ model (Jutzi et al. 2008) with a relatively small crushing strength ($P_{cr} = 10$ MPa), which may be a lower bound for materials analog to Dimorphos'. With the use of the basalt-like material model, which defines a grain density of $\rho_G = 2650$ kg/m^3, the bulk density, ρ_B, is given as 1600 kg/m^3.

The DART impact on Dimorphos in the gravity regime is the end-member of the expected impact condition, which is comparable to the artificial crater formation on Ryugu demonstrated by Hayabusa2's SCI impact (Arakawa et al. 2020). Within this regime, cohesionless surface and subsurface layers may make the impact process sub-catastrophic, where the target body significantly changes its shape but does not experience catastrophic disruption (e.g., Jutzi 2019). SPH simulations for up to ∼2 h after the DART impact reveal that for weak asteroid targets with $C_0 < 10$ Pa, a DART-like impact creates morphologies dissimilar to a typical impact crater but induces significant shape deformation. Figure 1 shows the initial target shape, a spherical, 150 m diameter body with $C_0 = 0$ Pa and $\theta = 31°$, and the shape 2 h after a vertical DART-like impact on it. The original target shape is assumed for simplicity of investigations. The deformation may reach the axis change up to ∼30 m along the impact direction.

SPH simulations also predict variations in the net momentum of ejecta depending on the target cohesion. For example, for an impact on targets with $C_0 > 10$ Pa, most ejecta acquire speeds higher than Dimorphos' escape speed, 0.1 m/sec. On the other hand, a lower C_0 leads to more ejecta below the escape velocity and larger redistribution of material within the body, giving an overall shape change.

Previous studies (e.g., Housen et al. 2018) also predict that the target crushing pressure affects the net momentum of ejecta. When this quantity is high, energy loss due to material crushing is less, causing an efficient energy transfer to materials' dynamics and thus more ejecta with higher speeds. For a smaller crushing pressure, a larger fraction of target materials can escape from the target, compared to a target with a larger crushing pressure and the same C_0.
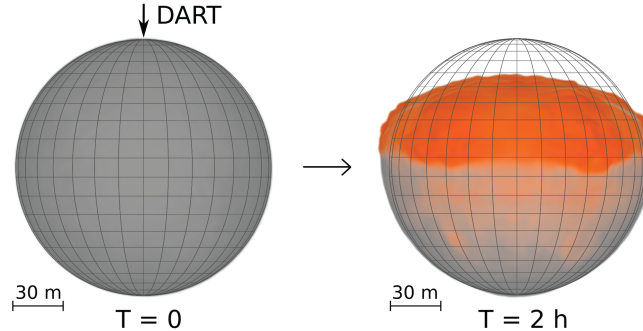

Figure 1 Initial (left) and final (right) asteroid morphology derived from an SPH simulation of a vertical DART-like impact on a spherical, 150 m diameter body with $C_0 = 0$ Pa and $\theta = 31°$. The orange regions indicate materials transported from their original locations to new places due to the DART impact. The bulk density, ρ_B, is 1600 kg/m^3.

2.2. *Rotationally driven reshaping on Didymos*

Top-shaped asteroids, or relatively spheroidal bodies with unique equatorial ridges, rotate with relatively short spin periods and are common in near-Earth asteroids (NEAs) (Taylor et al. 2012; Benner et al. 2015). Because many top shapes like the primary of (66391) Moshup, an S-type system formally known as 1999 KW4 (Ostro et al. 2006), are uniquely axisymmetric (e.g., Benner et al. 2015), the preferred explanation is that they might result from rotational reshaping (e.g., Walsh et al. 2006; Harris et al. 2009). Some top-shaped NEAs including Moshup host smaller satellites (e.g., Becker et al. 2015; Naidu et al. 2015), suggesting that top-shape formation and evolution strongly correlate with binary and multiple system formation (Margot et al. 2015; Walsh & Jacobson 2015). Such formation processes cause their unique evolution cycles (Jacobson & Scheeres 2011; Jacobson et al. 2016).

Detailed observations of asteroids (101955) Bennu and (162173) Ryugu by OSIRIS-REx (Lauretta et al. 2019) and Hayabusa2 (Watanabe et al. 2019), respectively, broadened discussions about the formation and evolution mechanisms of top shapes such as rotational reshaping (Hirabayashi et al. 2019b, 2020a; Cheng et al. 2020), catastrophic disruption of parent bodies followed by reaccumulation of debris (Michel et al. 2020), and accumulation of ejected debris while bodies span at fast rotation (Hirata & Ikeya 2021). Unlike other top shapes, however, Bennu and Ryugu are not fast rotators; Bennu's spin period is 4.296 h (Nolan et al. 2019; Hergenrother et al. 2019), while Ryugu's is 7.63 h (Watanabe et al. 2019). If rotation indeed plays a crucial role in their top shapes, the present spin states of these asteroids may not contribute to their rapid top-shape evolution, although surface material flows actively occur (Barnouin et al. 2019; Walsh et al. 2019; Jawin et al. 2020; Daly et al. 2020). If so, their dynamic spin evolution has enhanced their top-shapes in the past (Walsh et al. 2019; Hirabayashi et al. 2019b, 2020a).

Didymos is a top-shaped asteroid with a bulk density, ρ_B, of 2170 kg/m^3 (Naidu et al. 2020) and a spin period, T_{sp}, of 2.26 h (Pravec et al. 2006). This condition is near the $\sim$2.2 h spin barrier of a spherical rubble pile body with $\rho_B = 2200$ kg/m^3 (Pravec et al. 2008). This fast rotation causes strong centrifugal acceleration on its surface, particularly in the equatorial region. Therefore, at present, this asteroid may be close to or beyond its structural failure, i.e., a complete collapse, without mechanical strength to hold the entire structure (Naidu et al. 2020; Zhang et al. 2017, 2021). If so, the DART impact, which causes ejecta particles to fall onto this body's surface, may provide a unique situation that disturbs its surface. If the kinetic energy delivered to it is high, its shape configuration may change, enhanced by rotation. This section summarizes recent efforts in quantifying Didymos' force field, its structural conditions and reshaping mechanisms, the surface response to DART impact-driven ejecta falling, the probability of ejecta collisions with Didymos, and an approach to measure the magnitude of Didymos' reshaping.

2.2.1. *Correlations between gravity fields and material distributions*

This section discusses how Didymos' surrounding dynamic environment depends on its internal structure. We apply a mass concentration (mass-con) model that discretizes the mass distribution into a set of many small point masses (Soldini et al. 2020). The model accounts for the gravitational and rotational force fields surrounding Didymos by considering $T_{sp} = 2.26$ h and a constant volume of 2.54×10^8 m^3 with different bulk densities. The supplemental materials and data also provide the normalized gravitational coefficients for the spherical harmonic expansion model for the considered cases (Section S1). The following analyses only focus on the vicinity of Didymos, in which Dimorphos' gravity is assumed to be negligible.

Zero-velocity curves describe the orbital energy level of small objects within a considered system. They provide with qualitative information about the bounded particle dynamics under energy limits. Equation (1) defines a potential, denoted as Ω, that accounts for both gravitational and centrifugal effects in the frame fixed at Didymos (Murrary & Dermott 2000),

$$\Omega = -\frac{1}{2}\omega_{sp}^2(x^2 + y^2) + U_g \tag{1}$$

where $U_g < 0$ is the gravitational potential, and ω_{sp} is the spin rate. Using the mass-con model yields

$$U_g = -\sum_{i=1}^{N} \frac{Gm_i}{r_{ik}} \tag{2}$$

where G is the gravitational constant, m_i is the ith point mass within the set of N particles characterizing Didymos' mass distribution. r_{ik} is the distance between the ith particle and a considered location. In the rotating frame, the x axis corresponds to the longest principal axis, the y axis is along the intermediate axis, and the z axis is along the shortest axis, which also corresponds to the spin axis. Ω may possess local maxima or saddle points, depending on ω_{sp}. These points are the so-called dynamic equilibria, where the net acceleration becomes zero. The Ω level exhibits energy ridges crossing these equilibria and surrounding the dynamic environment (Murrary & Dermott 2000). Inside the ridges, a particle's dynamics is bounded, given Ω. On the other hand, if particles are outside the ridges, the motion is unbounded.

Figure 2 shows the zero-velocity curves surrounding Didymos on its equatorial plane; each contour shows the same Ω level. Figure 2a gives the case of the nominal bulk density, which is $\rho_B = 2170$ kg/m^3. There is only one equilibrium point (EQ1), which is linearly stable and almost touches the surface at the concavity. Particles resting initially but later ejected from this region may stay there because this stable equilibrium point may keep them trapped. On the

other hand, other equatorial areas do not host equilibria and are outside the energy ridges, causing material shedding rotational acceleration exceeding gravitational acceleration and thus unbounded motion. Figure 2b depicts the case of $\rho_B = 1820$ kg/m^3. A lower bulk density than the nominal case results in lower gravity acceleration while the rotational acceleration remains unchanged. This leads to dominant rotational effects in the surrounding area and so no existence of equilibria. On the other hand, if $\rho_B = 2520$ kg/m^3, the gravitational effect becomes higher, giving the presence of more equilibria (Figure 2c). Eight equilibria may surround the body for this case. Four equilibria (EQ1, EQ3, EQ5, and EQ7) are linearly stable, while the other four (EQ2, EQ4, EQ6, and EQ8) are unstable.

The results show that particles resting on the equatorial surface are in general susceptible to ejection due to a high rotational effect. Even the nominal bulk density case gives a condition that particles may be shed if no attractive force keeps them on the surface. This finding implies that if particles are cohesionless, they cannot rest on the surface and may tend to move towards the equator, and some may depart from the surface (Yu et al. 2018). As shown below, this rotational sensitivity directly correlates with the internal structure (Section 2.2.2).
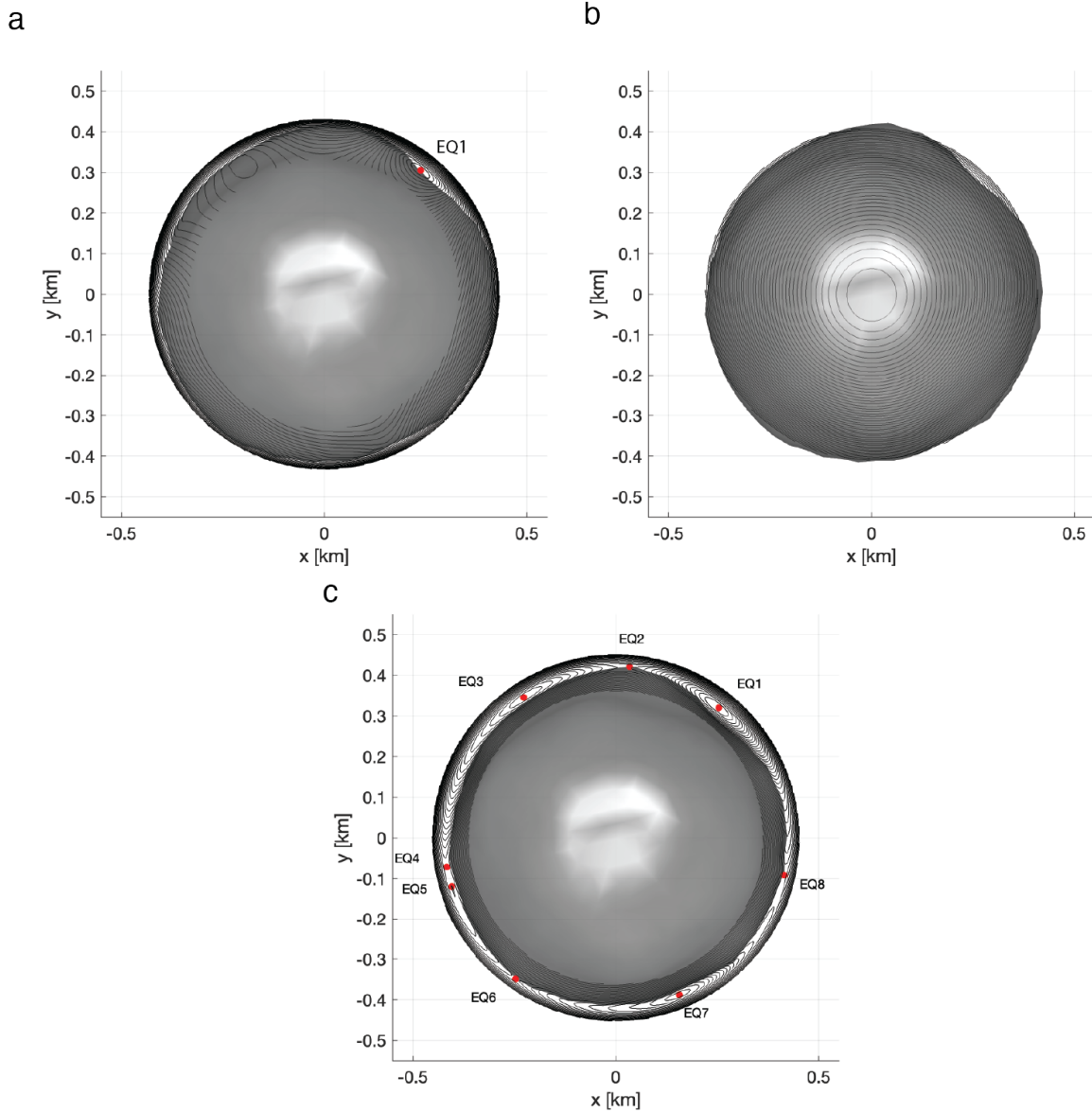
Figure 2 Zero-velocity curves on the equatorial plane with three bulk densities. a. $\rho_B = 1820$ kg/m^3. b. $\rho_B = 2170$ kg/m^3. c. $\rho_B = 2520$ kg/m^3.

2.2.2. *Present structural conditions*

This section examines Didymos' current structural condition by applying a semi-analytical approach (Nakano & Hirabayashi 2022). The parameter used here is the critical cohesive strength, C_{crit}, which defines the minimum cohesive strength that the body should possess to remain structurally intact (Hirabayashi 2015). If a structural element has its actual cohesive strength lower than C_{crit}, it should fail structurally and experience inelastic deformation. Depending on where and how this condition appears, the magnitude of reshaping varies (Hirabayashi 2015). Details are provided in Section 2.2.3).

The semi-analytical approach yields the spatial distributions of C_{crit} within Didymos. Assuming that the internal structure is uniform, this approach calculates the stress distributions by solving the equilibrium stress equation with the traction boundary conditions (Nakano & Hirabayashi 2022). The computed stress distributions are then applied to the Drucker-Prager yield criterion [ref] to determine C_{crit} at a given location. The angle of internal friction, θ, is fixed at $35°$, based on study reporting the properties of terrestrial materials (Lambe & Whitman 1969).

This approach is applied to compute C_{crit} for Didymos at $T_{sp} = 2.26$ h. The asteroid is assumed to be a uniformly rotating triaxial ellipsoid with a dimension of 837 m $\times$ 832 m $\times$ 786 m[1]. Figure 3 illustrates the spatial distribution of C_{crit} on the asteroid's cross-section with the three bulk densities discussed in Section 2.2.1, i.e., 1820 kg/m^3, 2170 kg/m^3, and 2520 kg/m^3. C_{crit} is always positive in the interior and on the surface at lower altitudes for all the bulk densities. This outcome suggests that cohesionless materials cannot support the current structure. When inelastic deformation spreads over these regions, the body cannot support its shape and eventually experiences a complete breakup (Zhang et al. 2017, 2021). However, this breakup scenario contradicts the current configuration (i.e., the body exists without failure), meaning that this body should have bulk cohesive strength.

While C_{crit} varies with ρ_B, the distribution trends remain unchanged. In other words, the inside always has the highest necessary cohesive strength, while surface regions have lower necessary cohesive strength. At the pole, on the other hand, major areas have negative distributions, meaning that no cohesive strength is necessary to keep these regions structurally intact. Therefore, C_{crit} within the considered bulk density range, $\rho_B = 2170 \pm 350$ kg/m^3, is about 20 to 30 Pa. If the actual cohesive strength is lower than that value at the central regions of this body, the body should fail structurally.

2.2.3. *Reshaping mechanisms*

Sections 2.2.1 and 2.2.2 suggest that Didymos needs mechanical strength. This interpretation is consistent with earlier work (Zhang et al. 2017; Naidu et al. 2020), though a low-strength structure may be suitable for rubble pile bodies given their formation and evolution associated with collision and reaccumulation (Richardson et al. 2002). The next key question is how Didymos ends up with reshaping if the body does not support the current configuration any longer. This section overviews Didymos' reshaping modes at $T_{sp} = 2.26$ h, given different interior conditions, by employing two Discrete Element Modeling (DEM) tools: `pkdgrav` (Schwartz et al. 2012; Zhang et al. 2017, 2021) and `GRAINS` (Ferrari et al. 2017, 2020). A key finding is consistent with earlier work showing that the reshaping mode driven by rotation strongly depends on the cohesive strength, density distribution, and particle arrangement and size distribution (Zhang et al. 2021; Hirabayashi 2015).

If the internal structure is homogeneous, and the van der Waals force is a primary factor of cohesion (Scheeres et al. 2010), boulders and gravels require substantial interstitial fine grains to bridge with similarly sized particles and stabilize the rubble pile structure (Sánchez & Scheeres 2014). Simulations by the `pkdgrav` code suggest that the critical cohesive strength, C_{crit}, of a homogeneous Didymos-like structure with $\rho_B = 2170$ kg/m^3 ranges from $\sim$11 Pa to $\sim$17 Pa (Zhang et al. 2021), consistent with those by the semi-analytical model above (Section 2.2.2) and a FEM study that predicted $\sim$20 Pa (Naidu et al. 2020). This cohesion level implies that Didymos needs grains with sizes smaller than 10 μm (Sánchez & Scheeres 2014). Figure 4 shows `pkdgrav` simulations that describe reshaping modes with randomly distributed particles ($\sim$4 - $\sim$ 16 m in diameter). They consider three bulk densities, $\rho_B = 1820$ kg/m^3, $\rho_B = 2170$ kg/m^3, and $\rho_B = 2520$ kg/m^3, and their C_{crit} values.

---

[1] The original dimension is 832 m $\times$ 837 m $\times$ 786 m (Naidu et al. 2020), we reorder it to avoid numerical issues in the semi-analytical model that uses elliptic integrals to compute the stress field.
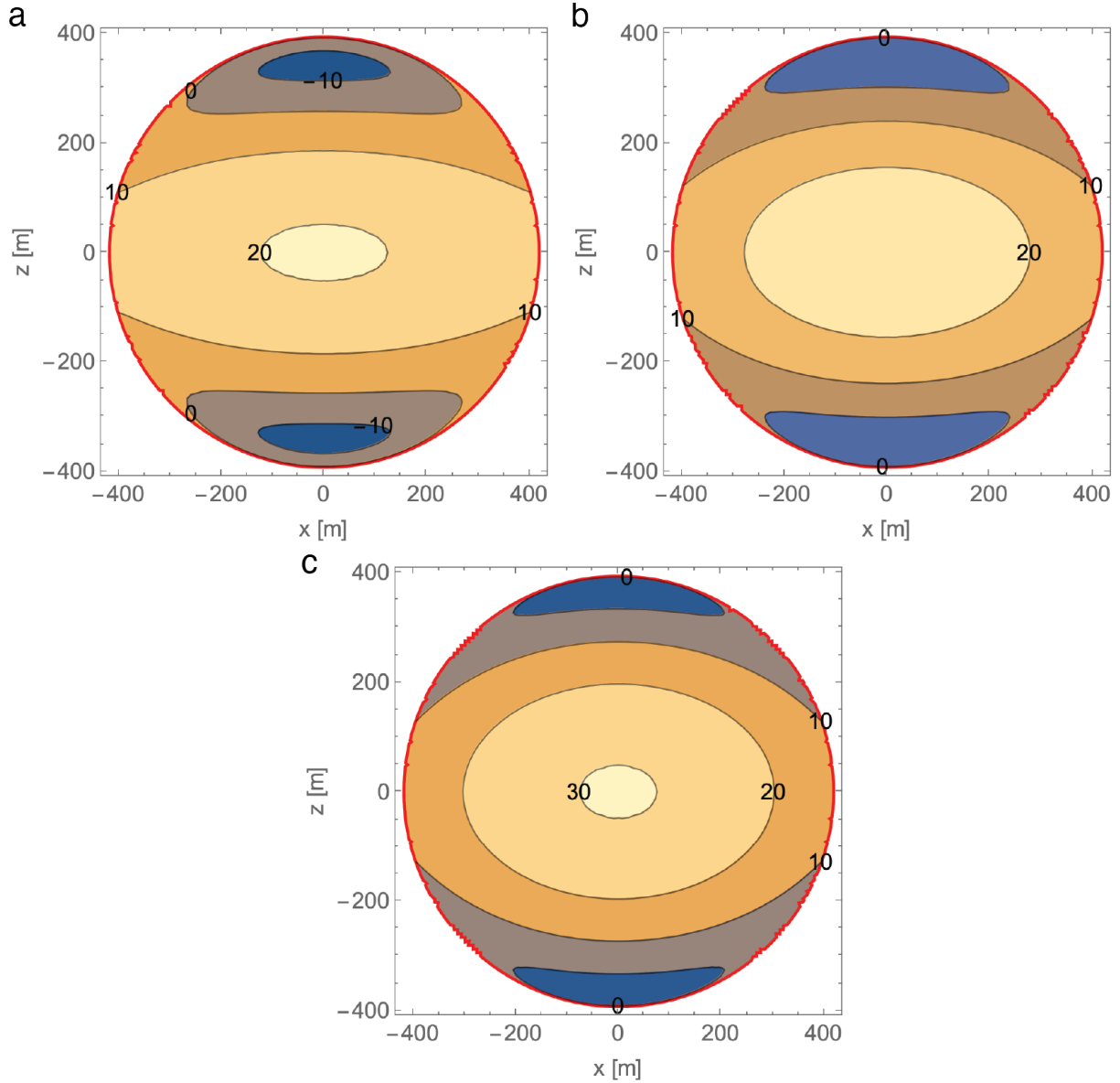
Figure 3 Spatial distributions of critical cohesive strength, C_{crit}, with different bulk densities. The angle of internal friction, θ, is 35°. a. $\rho_B = 1820$ kg/m³. b. $\rho_B = 2170$ kg/m³. c. $\rho_B = 2520$ kg/m³. For all the cases, the shape considered has a dimension of 837 m × 832 m × 786 m. The analysis applies the DRA parameters, identical to the measured extends along the principal axes (Naidu et al. 2020), to compute the stress distributions. This process leads to a ∼10% variation in volume, although this discrepancy does not affect the final results.

When $\rho_B = 2170$ kg/m³, the interparticle cohesive strength, c, should be higher than 330 Pa to maintain global structural stability. If c is less than that, the internal and surface regions fail almost simultaneously. Figure 4b shows the reshaping mode when $c = 320$ Pa. The resulting reshaping process yields a pancake-like shape. When $\rho_B = 1820$ kg/m³, and $c = 710$ Pa to maintain global structural stability; otherwise, the structure would be unstable (Figure 4c). The resulting reshaping process is a breakup because the internal structure is the most sensitive to structural failure at this rapid spin state (Section 2.2.2) and the large interparticle cohesive strength makes the body brittle and break easily after the internal structure fails. The split components are relatively large because of cohesive strength still connecting particles while global fractures propagate through the global shape. If $\rho_B = 2520$ kg/m³, the c value should be higher than 160 Pa to avoid reshaping. If $c = 150$ Pa (Figure 4d), the reshaping mode mainly consists of surface material movements.
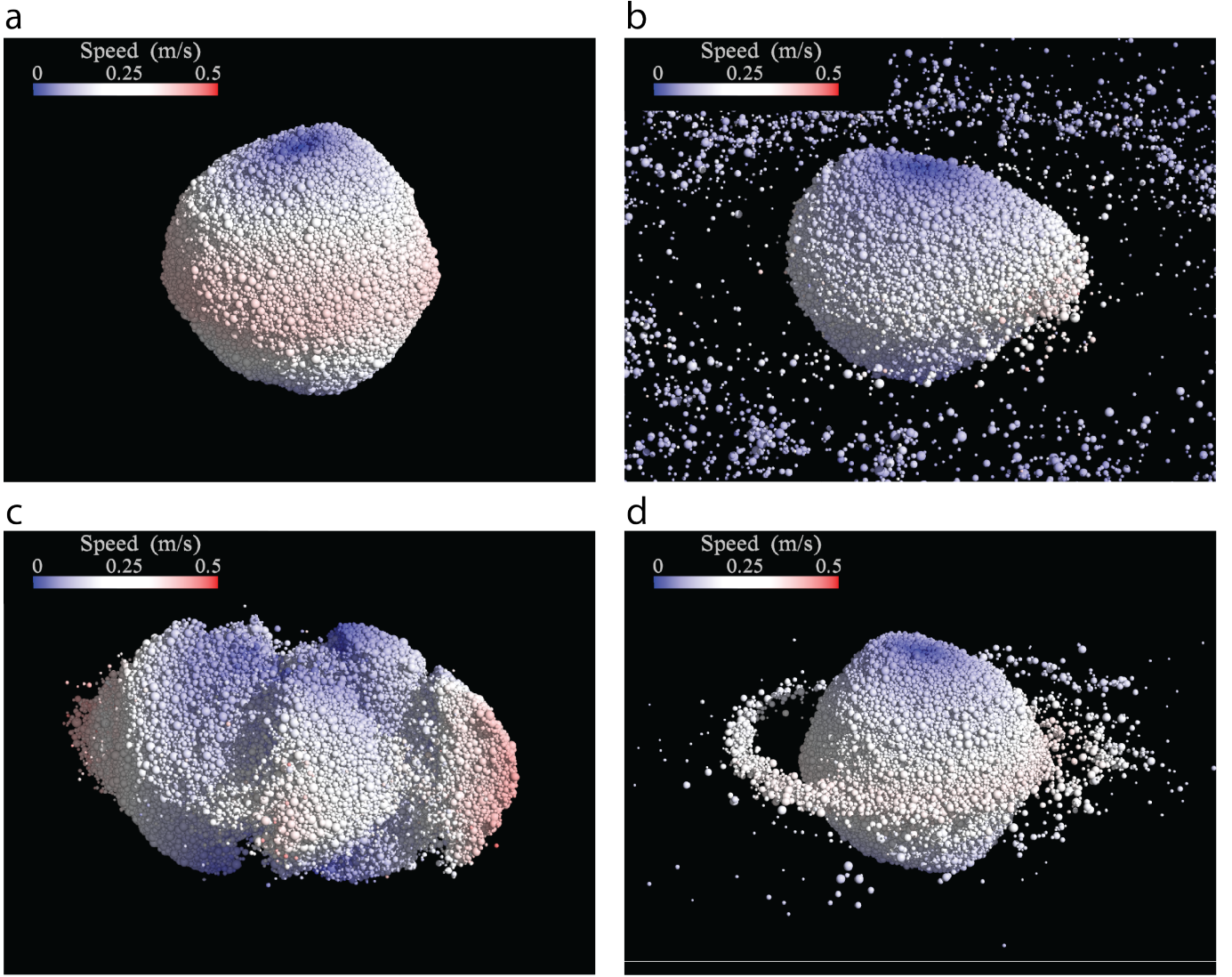
Figure 4 `pkdgrav` simulations showing Didymos' reshaping modes depending on the interparticle cohesive strength, c, and the bulk density, ρ_B. The particle size distribution ranges between ~ 4 m and ~ 16 m. The color shows the particle speed. a. Original shape configuration. b. $c = 320$ Pa and $\rho_B = 2170$ kg/m^3. c. $c = 700$ Pa and $\rho_B = 1820$ kg/m^3. d. $c = 150$ Pa and $\rho_B = 2520$ kg/m^3.

Figure 5 illustrates `pkdgrav` simulations exploring larger parameter space (Zhang et al. 2021). The results show that if ρ_B increases, C_{crit} becomes lower. This behavior stems from the increase in the gravitational effects, lending to a more structurally stable configuration. The lower-density case ($\rho_B <\sim 2170$ kg/m^3) leads to tensile failure, while the higher-density case ($\rho_B \geq\sim 2170$ kg/m^3) results in surface shedding and internal deformation (Zhang et al. 2021). Furthermore, the internal structure variations change C_{crit} up to 30%. The slope of the C_{crit} variation for a hexagonally packed configuration is higher than that for polydisperse cases. A well-organized structure like a hexagonally packed configuration may be more fragile when the tensile stress becomes dominant while supporting its structure under a stronger gravitational influence without cohesive strength. On the other hand, the polydisperse configuration needs a lower cohesive strength than the hexagonal packing configuration when the bulk density is low.

Recent in-situ observations of top-shaped asteroids Bennu and Ryugu inferred their mechanically weak surface structures (Scheeres et al. 2020; Arakawa et al. 2020; Roberts et al. 2021). If Didymos has a similar heterogeneous structure consisting of a weaker surface layer and a relatively stronger interior, the major reshaping process is surface mass movements (Ferrari & Tanga 2022). Figure 6 illustrates simulations from the `GRAINS` code to show how the existence of a mechanically strong core changes the reshaping mode. The strong inner core defines the presence of
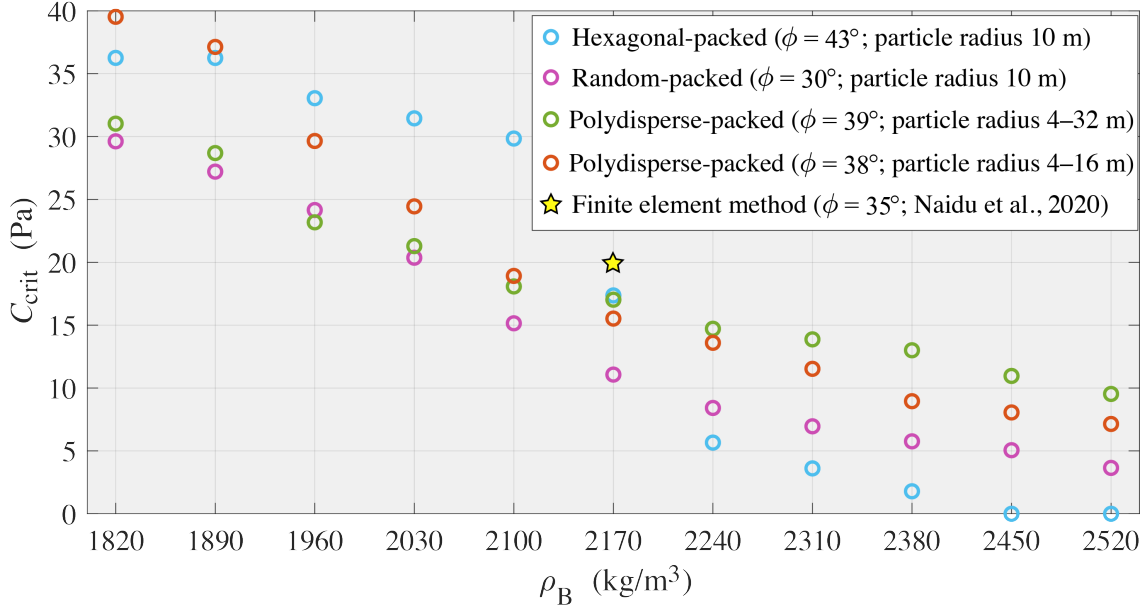
Figure 5 Critical cohesive strength C_{crit} with respect to the bulk density ρ_B for four homogeneous rubble-pile structures (adapted from Figure 12 in Zhang et al. 2021).

non-deformable volume within the asteroid's internal structure and may be made of one single monolithic block or a set of multiple large blocks.

If the volumetric ratio of the strong core to the entire body, ψ_c, is about 50%, and $\rho_B = 2170$ kg/m³ (Figure 6a), the reshaping mode consists of the formation of a small ring close to the equator with approximately 3.6% of Didymos' total mass. If $\psi_c = 25\%$ and $\rho_B = 2170$ kg/m³ (Figure 6b), the asteroid deforms to enhance its equatorial ridge. A smaller strong core causes Didymos to experience large reshaping and a mass loss. For example, if $\psi_c = 10\%$ and $\rho_B = 2520$ kg/m³, the reshaping mode is significant, leading to substantial mass ejection from the equator (Figures 6c and 6d). When a uniform density body consists of a mechanically weak surface layer and a strong core, mass ejection may reach only 1.2% of the total mass (Figure 6c). On the other hand, when the asteroid has a denser inner core with a density of 4236 kg/m³ and an underdense surface layer with a density of 502 kg/m³ and a low mechanical strength (Figure 6d), mass ejection may reach about 18.0% of the total mass (Figure 6d).

These results show that a higher ψ_c prevents global deformation but allows surface material movements, causing exposure of mechanically strong areas at the poles. For a very high ψ_c value, particularly larger than 50%, the global shape can remain almost intact even when the external layer is made of cohesionless materials because of interlocking between irregular grains (Ferrari & Tanga 2022). Otherwise, the resulting mass movements on the surface enhance the equatorial ridge. This finding is consistent with earlier numerical and theoretical analysis (Hirabayashi 2015; Hirabayashi et al. 2015; Zhang et al. 2017).

2.2.4. *Reshaping after the DART impact*

The DART impact creates particle ejection with various speeds. For the nominal case, while fast particles in the ejecta plume escape from the Didymos system, some low-speed particles may return to Dimorphos or hit Didymos. This section discusses how such slow particle collisions influence the surface conditions on Didymos.

Impact simulations are carried out using the GDC-i code, a soft-sphere DEM code for simulating impacts at various velocities (Sánchez Lana & Scheeres 2018). This simulation tool considers granular beds to mimic Didymos' surfacing environment at different latitudes, assuming that the body shape is spherical. The granular bed is $1\,\text{m} \times 1\,\text{m} \times 0.8\,\text{m}$ in size and consists of 60000 spherical particles. The particle size distribution ranges between 1 cm and 3 cm, and the grain density, ρ_G, is 3400 kg/m³. The test bed structure has porosity of $\phi_0 = 0.36 - 0.37$ and avoids crystallization. Also, the angle of internal friction, θ, is set to be $\sim$35°. Particles at the bottom of the container are kept motionless, and the container has periodic boundary conditions in the horizontal direction. The gravitational acceleration on Didymos is 2.32×10^{-4} m/s² and changes its direction at a simulated latitude that causes different rotational effects.
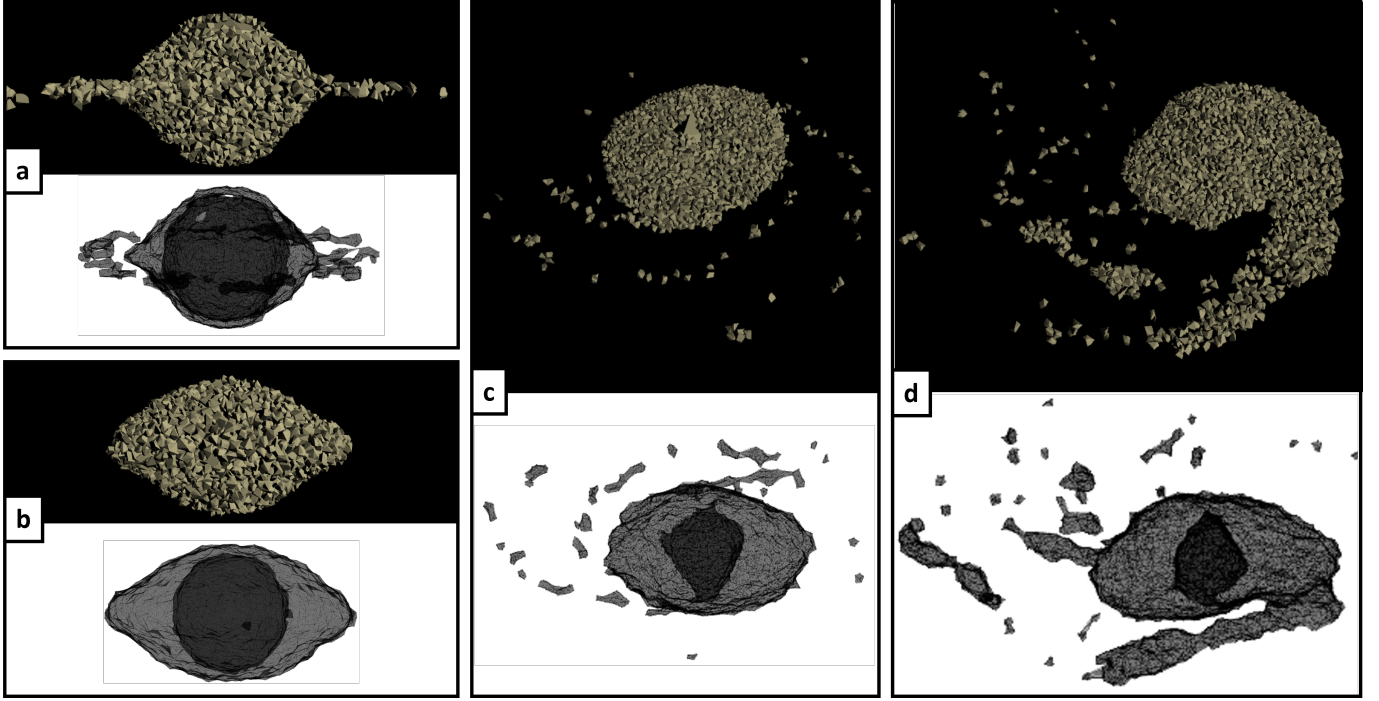
Figure 6 `GRAINS` simulations showing Didymos' reshaping modes depending on the bulk density, ρ_B, and the volumetric ratio, ψ_c. The mass ejection ratio, M_e, defines a ratio of the ejected mass to the total mass. The particle size is on the order of ~ 10 m. For each panel, the upper figure is the external view, while the lower figure illustrates the inner structure with a dark region identifying the inner stronger core surrounded by a transparent layer of fragmented material. a. $\psi_c = 50\%$ and $\rho_B = 2170$ kg/m^3, leading to $M_e = 3.6\%$. b. $\psi_c = 25\%$ and $\rho_B = 2170$ kg/m^3, leading to $M_e = 0.04\%$. c. $\psi_c = 10\%$ and $\rho_B = 2520$ kg/m^3, leading to $M_e = 1.2\%$. d. $\psi_c = 10\%$ and $\rho_B = 2520$ kg/m^3, leading to $M_e = 18.0\%$.

The bulk cohesive strength, C_0, is initially 25 Pa everywhere and then lowers to 0 Pa in the region affected by the collisions. The projectiles, i.e., ejecta particles coming from the DART impact site, are spheres with a diameter of 10 cm and the same density as the surface particles ($\rho_G = 3400$ kg/m^3), leading to a mass of $M_{ejc} = 1.78$ kg. Each experiment uses the same granular bed, shoots the same impactors five times at an interval of 2 s with the same impact speed, and continues with no further impacts for 290 s (Figure 7).

Figure 8 shows the average speed of surface particles in the horizontal plane, V_x, 12 s after a shot of the last projectile with two impact speeds: $V_{ejc} = 1$ m/s (Yu & Michel 2018) and $V_{ejc} = 5$ m/s. The results show that for $C_0 > 25$ Pa, mass movements on a large scale are unlikely to occur even for successive impacts five times. There is no significant particle movement ($\sim$ mm/s) below the top surface (about the 0.8 m line), whereas particles above the surface have acquired speeds an order of magnitude smaller than the impact speed. These simulations conclude that the surface condition with $C_0 \geq 25$ Pa and $V_{ejc} \leq 5$ m/s is enough to avoid disturbance on Didymos' surface. However, if $C_0 < 5$ Pa, which is comparable to C_{crit} at middle and high latitudes, impact-induced mass movements may happen for $V_{ejc} \geq 1$ m/s.

2.2.5. *Influences of ejecta speed and cone geometry on their collisions with Didymos*

The remaining issue is whether the DART-driven ejecta deliver high kinetic energy to Didymos. A simple statistical model characterizes how the collision conditions of the DART-driven ejecta with Didymos changes due to the surface slope uncertainties. The present study only focuses on the ejecta traveling faster than the escape speed of the Didymos-Dimorphos system, i.e., ~ 0.43 m/s^2[2], although the gravity effect from Didymos and Dimorphos is considered.

The model first determines the DART spacecraft condition and the locations and orientations of Didymos and Dimorphos at the impact event by using DRA via the SPICE tool. The script is written in Python and uses SpiceyPy

---

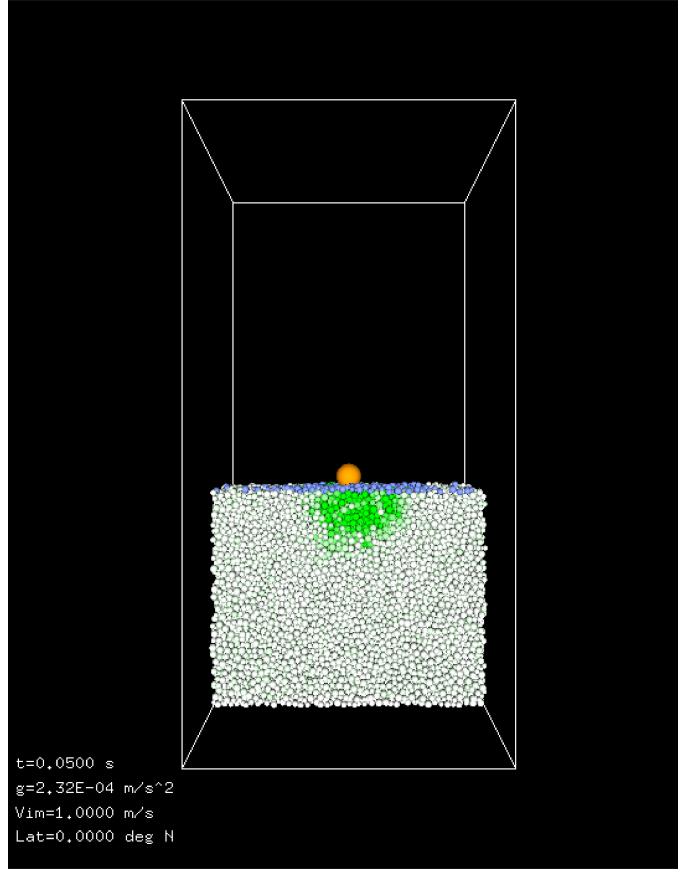[2] The escape speed is calculated assuming that a particle is sitting on Didymos' surface.

Figure 7 Simulation setup. The image shows a perpendicular impact at 1 m/s on a cohesive bed. The colour green is linked to the kinetic energy of the particles.
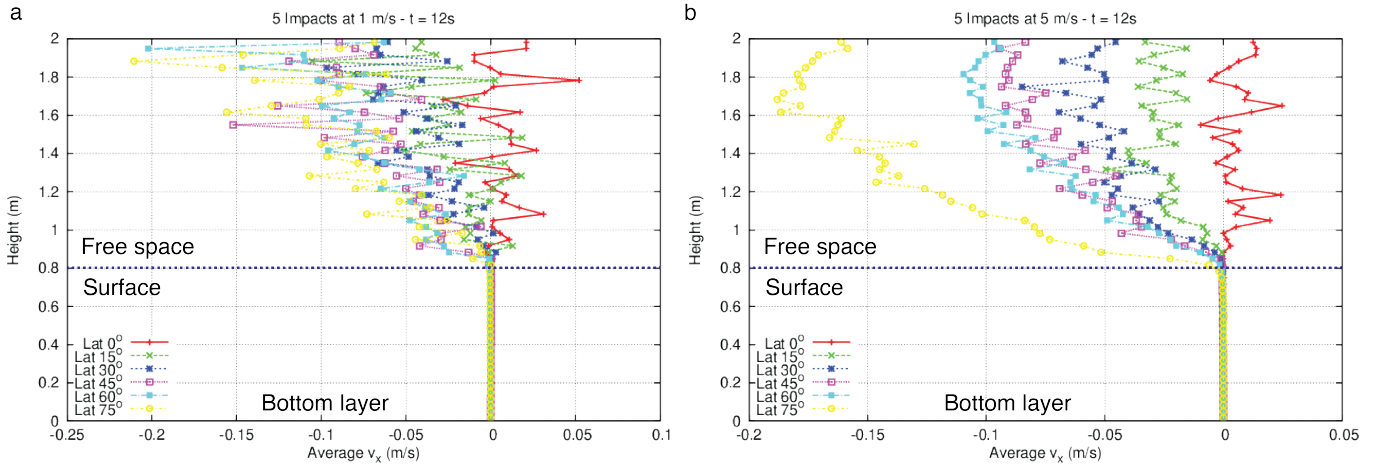

Figure 8 Velocity profile of the particles in the simulation box 12 s after the last projectile was shot. Each line corresponds to a different latitude. V_x is the velocity component along the horizontal component. The bulk cohesive strength is fixed at 25 Pa. The surface layer is located around 0.8 m from the bottom, and the regions above it is free space. a. $V_{ejc} = 1$ m/s. b. $V_{ejc} = 5$ m/s.

for the SPICE toolkit (Annex et al. 2020). Given the SPICE kernels available as of January 15, 2022, the expected impact time is at 23:14:18 on September 26, 2022 UCT. The impact out-of-plane angle is ~9.62°, and the impact speed

is 6.14 km/s, although these values are subject to change. The ejecta generation and cone geometry at this event are then computed by using the scaling relationship approach developed by Richardson et al. (2007) (also see a summary of their techniques in Appendix A). The ejection speed from the impact site constraints the estimated arrival time of the ejecta at Didymos and Didymos' orientation at that time. The model checks whether the ejecta hit Didymos. If the collision event happens, it records the event; otherwise, it moves onto the next runs without recording.

A total of 15000 test runs are performed to find statistical trends of the collision events. We use two uniformly random variables (declination and right ascension) to compute the surface normal at the DART impact site on Dimorphos. To define the updated surface for each test run, the model first defines the original surface normal. This original surface normal is then updated adding the random variables; the declination variation from the original surface normal, later denoted as the deviation angle, is limited at $45°$. In addition to the variations in the surface normal, we consider how the timing of ejection and the surface strength, which mainly control the ejection speed, affect the probability of the collision events. Three cases are considered. The first two cases represent when the impact condition is in the gravity regime with zero cohesion and have different timings of ejection. The first case assumes a timing of 5 s, which generates ejecta with an ejection speed of ~ 0.8 m/s, while the second case considers that of 0.1 s, which is equivalent to ~ 14 m/s. These cases represent relatively early stages of the crater formation, which may continue for about 760 s. The last case is when the DART impact occurs on a surface with a cohesive strength of 2000 Pa, and the timing of ejection considered is 0.1 s, which is equivalent to an ejection speed of 14 m/s. The crater formation timescale for this case is about 16 s.

Each case is examined with 5000 test runs. The first case finds that 386 runs are identified to encounter collisions, leading to a collision probability of $\sim 7.7\%$. The second case, on the other hand, has 660 collision events ($\sim 13.2\%$). The discrepancy of these cases results from the ejecta speed, which determines how long the ejecta travel to arrive at Didymos. Fast ejecta with a speed of ~ 14 m/s only take 1.5 min to arrive at the asteroid. Within this timescale, the contribution of Dimorphos' velocity to the ejecta motion does not affect the final destination much. On the other hand, slow ejecta with a speed of ~ 0.8 m/s arrive at Didymos ~ 25 min after the departure, and this asteroid's velocity is no longer negligible and causes a drift of the ejecta motion. Some particles may also be attracted to Didymos' gravity. Finally, given relatively fast ejecta, the third case also have 641 collision events ($\sim 12.8\%$).

Figure 9 shows the fractions of collision events and total cases as functions of the deviation angle and the impact angle. The collision events may occur if the deviation angle is higher than 17 degrees (Figure 9a). The fraction for the 0.1 s ejection timing cases (i.e., the second and third cases) is, in general, slightly higher than that for the 5 s ejection timing case (i.e., the first case). Again, this discrepancy results from the traveling time between Didymos and Dimorphos. Furthermore, the impact angle between $40°$ and $70°$ makes the collision events happen (Figure 9b). These results suggest that the ejection speed and surface slope angle are the major contributors to the probability of ejecta collision events on Didymos. On the other hand, ejecta slower than $\sim$m/s likely hit more frequently, but such events may occur after they orbit the system for a while (Yu et al. 2017; Yu & Michel 2018).

2.2.6. *Measurement of Didymos' reshaping*

The reshaping timescale may be characterized by considering how quickly particles on this asteroid move, given the acceleration that they experience. The duration that a particle moves over a distance of q from one location to another under constant acceleration of a is proportional to $(2q/a)^{0.5}$. While a varies significantly in the asteroid environment, using the acceleration at Didymos' equator, which is about 3.5×10^{-5} m/s^2, yields an upper timescale of ~ 1.7 h for a particle to move ~ 600 m, which is almost equivalent to a distance from the pole to the equator. This timescale is relatively shorter than the orbital period, 11.9 h. Within this reshaping timescale, Dimorphos only moves 51 deg of its phase angle, and its orientation and position do not change significantly. Given this condition, the angular momentum of Didymos' rotation is assumed not to be transferred to that of Dimorphos' dynamics and remain constant during the process.

As shown in sections 2.2.3, a reshaping event likely makes the body more oblate and increases its moment of inertia along with the z axis. Consequently, under a constant angular momentum, Didymos' spin period becomes longer. Figure 10 illustrates the variation in the spin period change as a function of the reshaping magnitude along the z axis. The variation is linear within the reshaping magnitude up to 10 m. A linear approximation function is obtained as $dT_{sp} = 21.5$ s/m dD, where dT_{sp} is a spin period change in seconds, and dD is the z axis length change in meters, i.e., $D_0 - D$, given the initial z axis length, D_0, and the post-reshaping z axis length, D (see discussions in Section 3.3 and Figure 12b). The asymmetric variations along the x and y axes do not give significant variations in the spin period
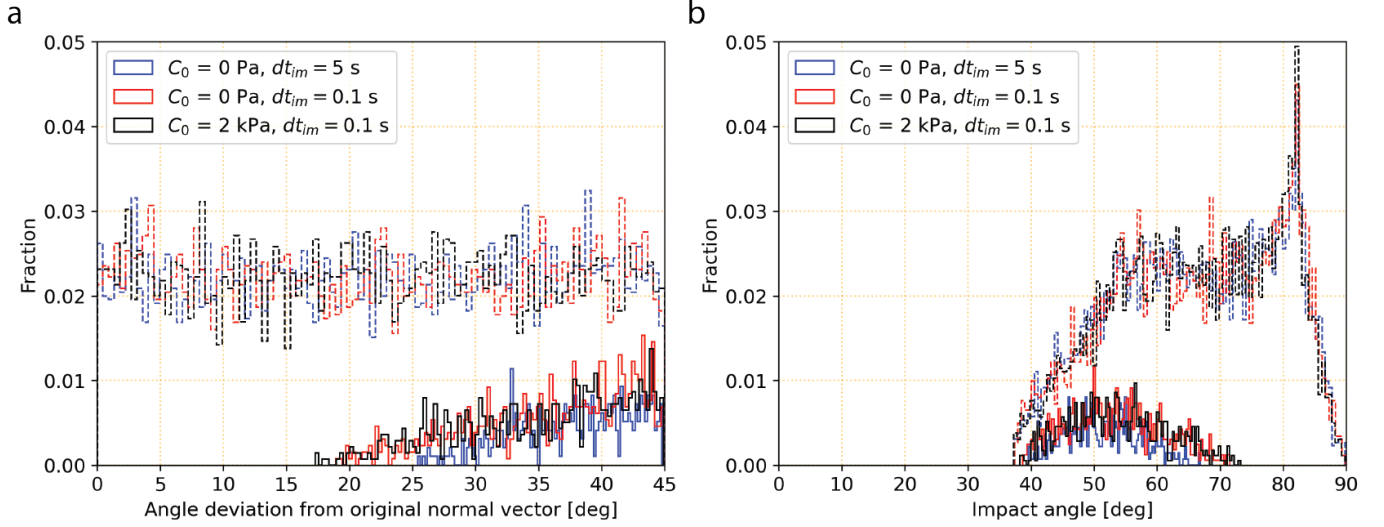
a

b

Figure 9 Fractions of collision events. a. Collision event fraction as a function of the deviation angles from the original surface normal. b. Collision event fraction as a function of the impact angle. The solid lines describe the collision events only, while the dashed lines show the total test runs. The fractions defined here are the ratios of the number of considered events to that of the test runs at a given point along the x axis.

change. The predicted uncertainty of photometric measurements for determining the spin period may be less than 0.1 s by the end of April 2023 [ref]. With this uncertainty, telescopic observations should be able to detect a reshaping mode with deformation of higher than 1 cm along the short axis (Rivkin et al. 2021).
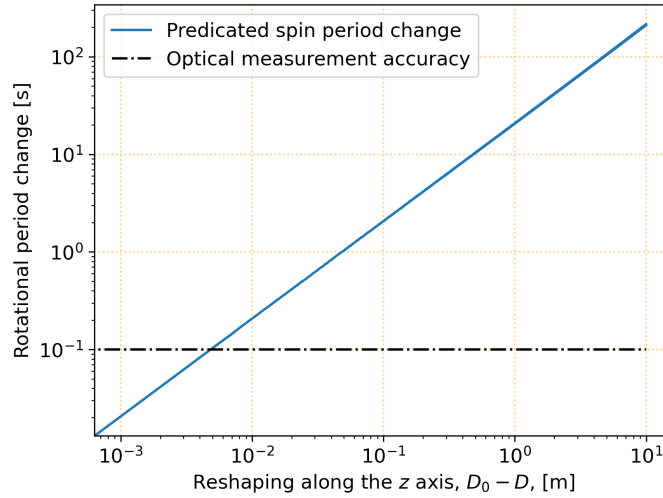
Figure 10 Didymos' reshaping driven spin period change. The x axis gives the reshaping-driven length change along the short axis, $dD = D_0 - D$, up to 10 m. The black dot-dashed line is the planned optical measurement accuracy obtained by the end of April in 2023.

3. RESHAPING CONTRIBUTIONS TO MUTUAL DYNAMICS

3.1. *Modeling the reshaping effects on orbital perturbation*

The reshaping processes on Dimorphos and Didymos change the mutual gravity field, giving additional orbital perturbation on top of the rigid-body behaviors (Hirabayashi et al. 2017, 2019a). The reshaping-driven orbital perturbation may be detectable by telescopic observations, depending on the reshaping scale. Nakano & Hirabayashi (2022) employ a dynamics model that simulates the motion of irregularly shaped bodies under mutual gravity interactions by using

a Finite Element Model (FEM) to formulate mutual potential and force computations (Yu et al. 2019). The study applies the radar shape model with an extended dimension of $832 \times 837 \times 786$ m^3 and a mass of 5.2280×10^{11} kg for Didymos and a tri-axial ellipsoid with a dimension of $208 \times 160 \times 133$ m^3) and a mass of 4.8417×10^9 kg for Dimorphos Naidu et al. (2020).

Nakano & Hirabayashi (2022) follow the approaches by Hirabayashi et al. (2017) and Hirabayashi et al. (2019a) to characterize the reshaping effects on orbital perturbation. The following two cases are considered to quantify the reshaping-driven orbital perturbation. First, the normal case is when the mutual dynamics in the Didymos-Dimorphos system is assumed to be in the relaxed state (Agrusa et al. 2021), and the asteroids' shapes are the original ones discussed above. Second, the second case is when either Dimorphos or Didymos experiences reshaping driven by the DART impact, though no DART impact-driven momentum affects the system's dynamics. As the present focus is on reshaping-driven orbital perturbation, this process effectively eliminates the contribution of the kinetic impact to orbital perturbation that causes Dimorphos to experience enhanced libration (Agrusa et al. 2021; Meyer et al. 2021). Based on the discussions in Section 2.2.6, the reshaping is assumed to occur instantaneously and keep the bodies' rotational angular momenta constant throughout the process. Specifically, the angular momentum for each component's rotation remains constant; the position and velocity of each body's center of mass remains unchanged, while the rotation varies because of the change in the moment of inertia. The orbital perturbation is assessed by subtracting the orbital motion for the normal case from that for the reshaping case. The following discussions denote the orbital phase angle for the reshaping case relative to the normal case as the relative angular position.

3.2. *Dimorphos' reshaping driven orbit perturbation*

This section discusses orbital perturbation resulting from the DART impact-driven reshaping on Dimorphos. The analysis assumes that this asteroid's mass is unchanged because the amount of the DART impact-driven ejecta is likely negligible compared to it. For simplicity, the following steps define Dimorphos' post-DART impact shape. First, the frame rotating with Dimorphos defines the orthogonal axes, $(\xi, \eta, \zeta)^T$, along the long, intermediate, and short axes, respectively (Figure 11a). The ζ axis is supposed to be identical to the spin axis. The η axis points towards the leading direction. The edge locations along the ξ, η, and ζ axes are $\pm\xi$, $\pm\zeta$, and $\pm\zeta$, respectively. The signs describe whether the edges are placed on the positive side or the negative side. .

The hypothetical DART impact occurs on the leading side of Dimorphos, implying that the reshaping may be axisymmetric along the η axis. Modeling Dimorphos' reshaping considers the variations in the edge locations before and after the DART impact. SPH impact simulations (Raducan & Jutzi 2022) (Figure 1) show that the DART impact deformation mainly happens in the $+\eta$ direction. Thus, the expected reshaping process is to make the $+\eta$ elevation lower than the original but keep the $-\eta$ elevation unchanged. The present model applies a rescaling process to the other two axes equally so that it satisfies the volume-constant condition. This reshaping process is characterized by considering the length change along the η axis, or $dL = L_0 - L$, where L_0 is the original length along the η axis and L is the post-impact length (Figure 11b).

Six cases simulated by Nakano & Hirabayashi (2022) demonstrate orbital perturbation with dL of up to 16 m. Simulations over 180 days suggest that Dimorphos' reshaping can cause additional orbital perturbation. Figure 11c illustrates the relative angular position with a time interval of 6×10^4 s when the length change of 16 m. While high-frequency oscillations occur mainly due to Dimorphos libration, the observed general trend is linear growth. After 180 days, the relative angular position reaches up to $85°$. As the time increases, Dimorphos' reshaping causes its position to be ahead of that in the normal case, leading to a shorter orbital period.

Figure 11d describes the orbital period changes for the considered cases as a function of the length change along the η axis. The results show that the reshaping processes shorten the mutual orbital period after the DART impact. Nakano & Hirabayashi (2022) also find that there are limited cases that the post-impact orbital period becomes longer. Furthermore, the trend of the orbital period change is linear. If the axis length change is ~ 2 m, the orbital period change reaches about 7.4 s, exceeding the 7.3 s measurement requirement. This magnitude may be approximately equivalent to when a 100 m diameter crater diameter, which is a predicted crater size in the gravity regime, forms after the DART impact (Nakano & Hirabayashi 2022).

3.3. *Didymos' reshaping driven orbit perturbation*

If Didyomos' reshaping is not negligible, this process also affects orbital perturbation. As discussed in Section 2.2.3, Didymos' fast spin may make the current axisymmetric shape more oblate if its structure reaches failure. Given the
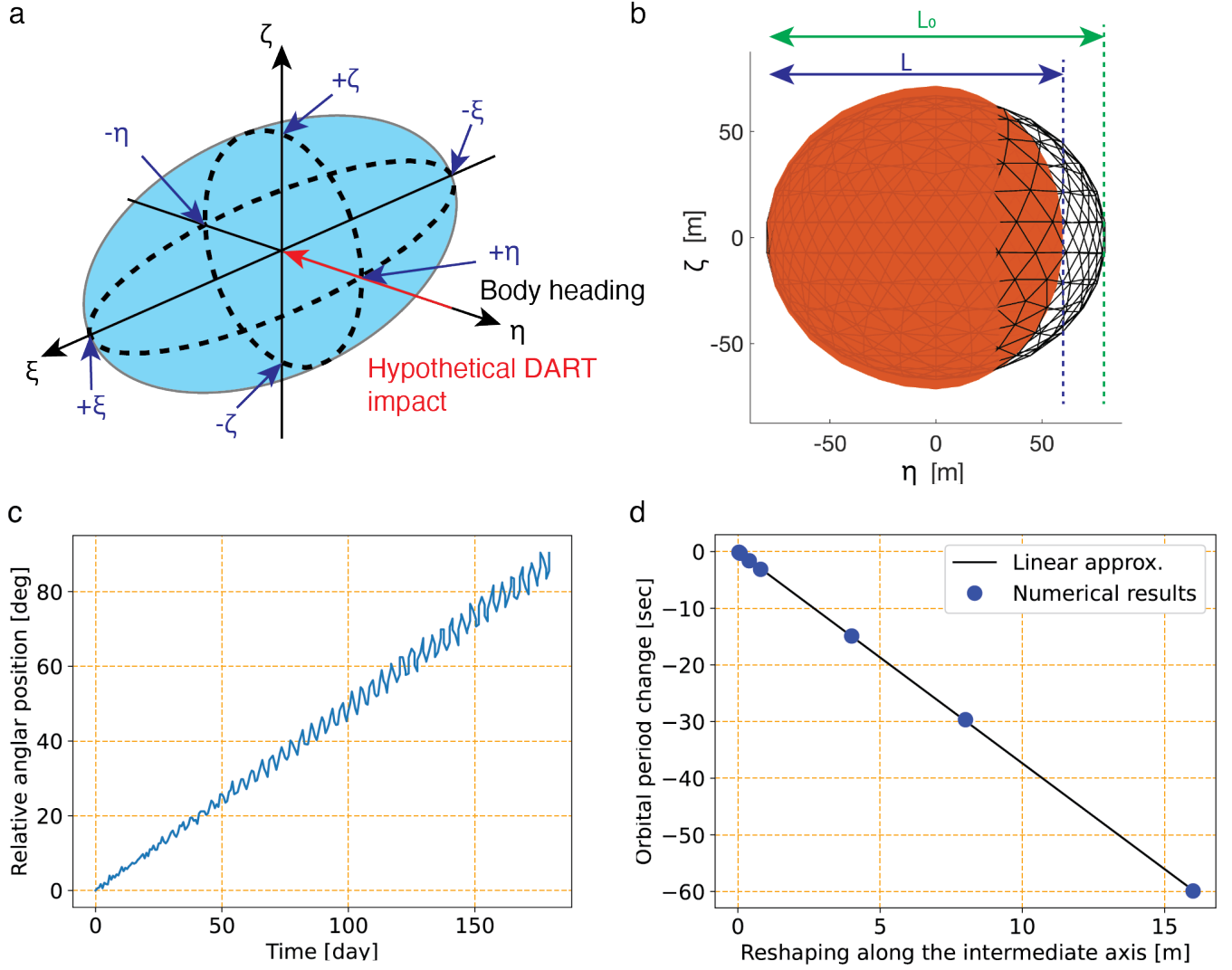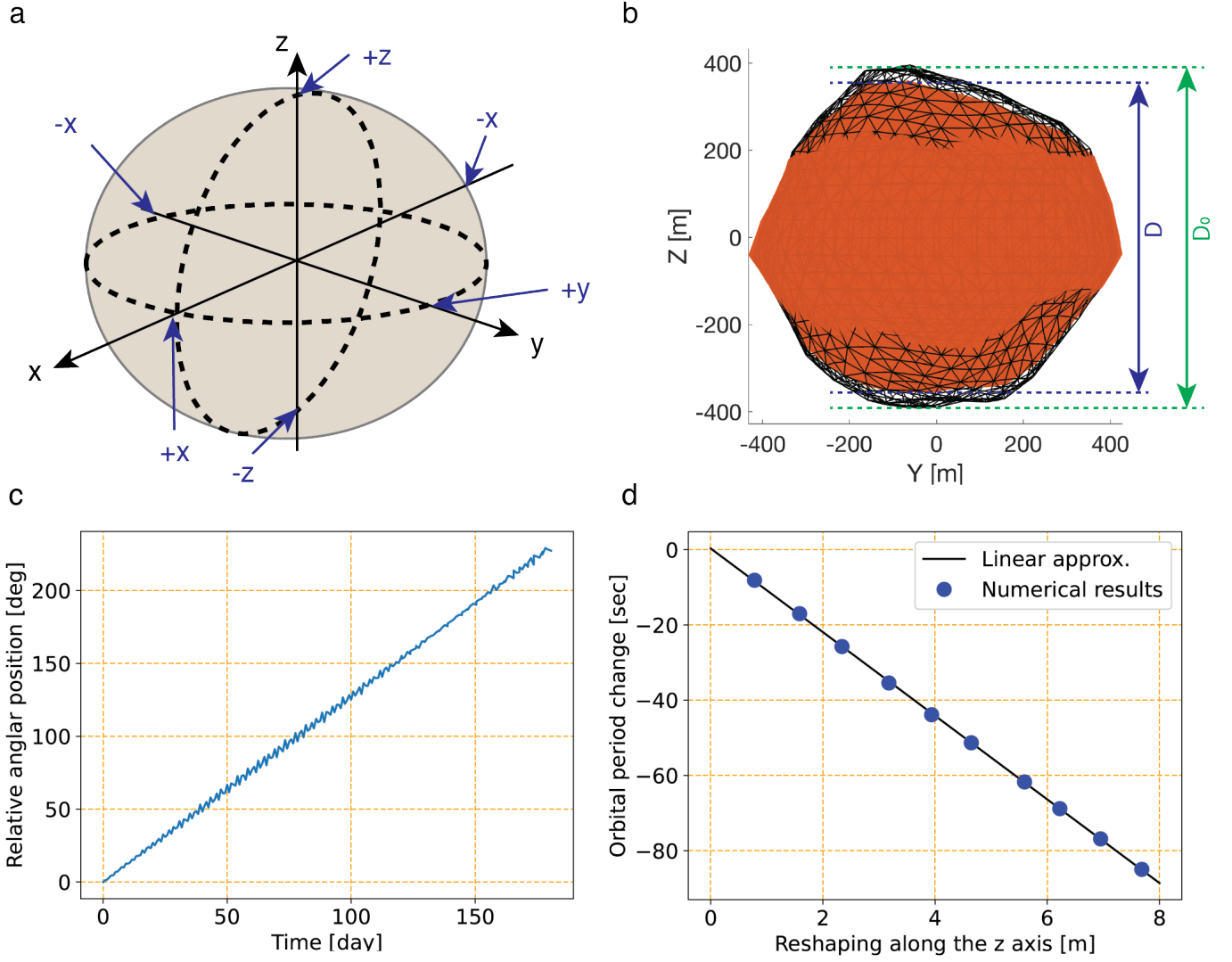
a

b

c

d

Figure 11 Dimorphos' reshaping mode and orbital perturbation. a. Defined coordinate frame. b. Example of reshaping. c. Time evolution of relative angular position with a length change of 16 m. d. Orbital period change with respect to length change.

coordinate frame (x, y, z), the reshaping mode shortens the short axis, $z_p - z_m$. Similar to Section 3.2, the signs define the locations of both positive and negative edges along each axis (Figure 12a). The total volume remains constant, given a process equivalently rescaling along the long axis, $x_p - x_m$, and the intermediate axis, $y_p - y_m$. Later, similar to Section 2.2.6, the change in the shortest axis, i.e., $dD = D_0 - D$, is used to define the magnitude of reshaping (Figure 12b).

Ten cases from Nakano & Hirabayashi (2022) show orbital perturbation when the short axis changes corresponding to ~0.8 m to ~8 m. Figure 12c shows the time evolution of the relative angular position over 180 days when the short axis change is ~8 m. Like Dimorphos' reshaping, the relative angular position grows linearly with time. Figure 12d illustrates that the orbital period becomes shorter linearly, with the reshaping magnitude. Didymos' reshaping can cause a larger orbital period change than Dimorphos' reshaping, given the same reshaping magnitude. This difference comes from the fact that Didymos plays a dominant role in controling the gravity field. A small change in Didymos' shape induces larger variations in the mutual dynamics. Given the 7.3 s measurement requirement, if the reshaping magnitude is higher than 0.7 m, Didymos' reshaping likely influences the β value measurement. The conclusion is consistent with Hirabayashi et al. (2017) and Hirabayashi et al. (2019a).

Figure 12 Didymos' reshaping mode and orbital perturbation. a. Defined coordinate frame. b. Example of reshaping. c. Time evolution of relative angular position with a length change of ∼8 m. d. Orbital period change with respect to length change.

4. DISCUSSIONS

4.1. *Reshaping-driven orbital perturbation*

This section illustrates potential scenarios of the reshaping-driven orbital perturbation by collecting discussions in the previous sections and their unresolved issues (Figure 14). The nominal DART impact scenario only considers an addition of the impact-driven kinetic momentum to Dimorphos' for the resulting orbital perturbation, which could be measured by using telescopic observations (Figure 14b). The predicted orbit period change for this case is at least ∼73 s (Rivkin et al. 2021).

However, the DART impact creates a crater on Dimorphos, while the ejecta orbit the system, some of which fall onto Didymos and may disturb its surface and interior (Figures 14c and 14d). While reshaping processes may (may not) occur on both asteroids, the major mechanisms are different (Figure 14c). Dimorphos' reshaping results from the cratering process. The crater size may strongly depend on the impact geometry and the surface and subsurface conditions (Section 2.1). On the other hand, Didymos' reshaping stems from its fast spin causing rotational acceleration. When the DART-driven ejecta hit Didymos' surface, the kinetic impact energy delivered by the ejecta to the surface

may disturb particles there. If the kinetic energy is high, particles move towards the equatorial regions, making the shape more oblate.

The reshaping processes on Dimorphos and Didymos give additional orbital perturbation. The reshaping processes pushes Dimorphos forward, inducing a shorter orbital period. Given the current scope of the reshaping magnitude (up to meters rather than complete disruption), the orbital period becomes linearly shorter with the reshaping magnitude. Within this range, the resulting orbit perturbation may exceed the telescopic detection limit (Rivkin et al. 2021). However, if it is larger than that reshaping scale, the orbital period variation evolves nonlinearly and significantly (Hirabayashi et al. 2017, 2019a).

One of the critical questions is whether these asteroids indeed experience reshaping processes that may cause detectable orbital perturbation. The answer to this question depends on their current geophysical and geotechnical properties, the DART impact on Dimorphos, and how DART impact-driven ejecta reach Didymos. The following focuses on whether the DART-impact driven reshaping occurs on Dimorphos and Didymos, with limited constraints on this problem. The present paper offers limited discussions about Dimorphos' DART impact-driven reshaping but refers to Raducan & Jutzi (2022).
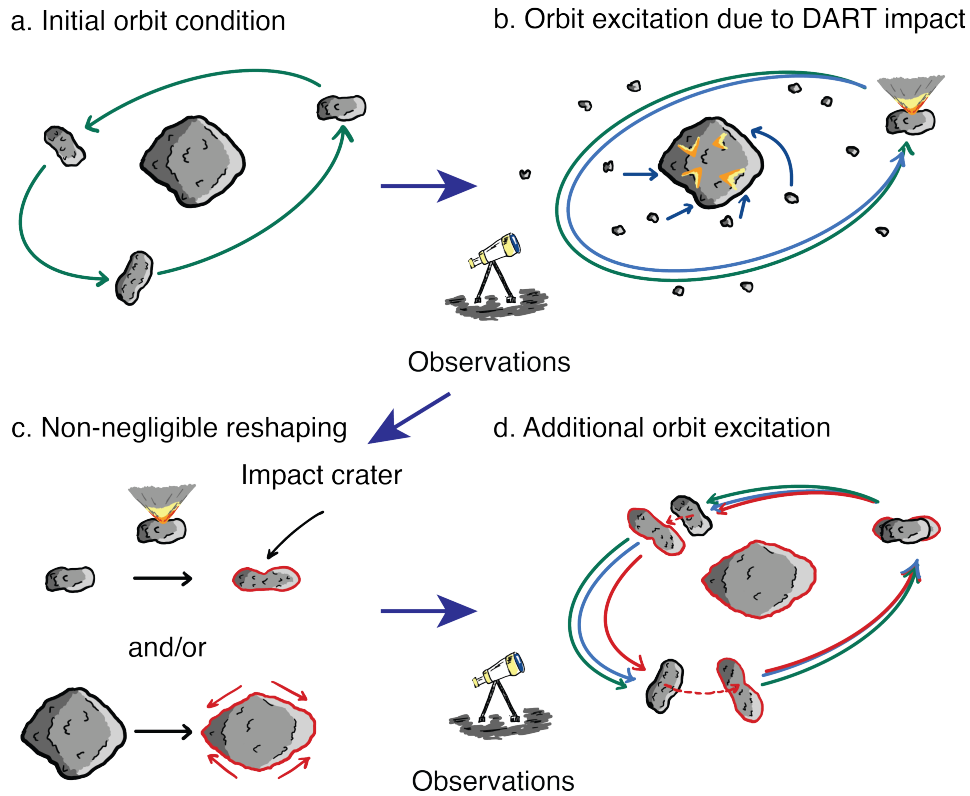
Figure 13 Reshaping-driven orbital perturbation. The green lines give the original orbit, i.e., the pre-impact orbit, the blue lines show perturbed orbits driven by the DART impact without reshaping, and the red lines describe those induced by the DART impact and the reshaping process. a. Pre-impact orbit. b. DART impact causing orbital perturbation without reshaping. c. Non-negligible reshaping happening to Dimorphos and Didymos. The shapes enclosed by black solid lines are the original shapes, while those by red solid lines are the deformed shapes. d. Reshaping-driven orbital perturbation.

4.2. *Dimorphos reshaping scenarios*

Recent space exploration missions demonstrated kinetic impact experiments on small bodies and inferred that the crater formation highly depends on the surface conditions. Deep Impact's kinetic impact experiment inferred that comet Tempel 1 might possess an effective strength of up to $1 - 10$ kPa (Richardson et al. 2007). On the other hand,

the Small Carry-on Impactor (SCI) experiment on Ryugu by Hayabusa2 revealed that the impact crater formation is likely in the gravity regime (Arakawa et al. 2020) on this asteroid's weak structure consisting of carbonaceous materials.

If the DART impact occurs in the gravity regime, similar to SCI on Ryugu, it may result in sub-catastrophic disruption. However, the Didymos-Dimorphos system's taxonomy is an Sg-type (de León et al. 2006; Rivkin et al. 2021), different from the carbonaceous types identified for Bennu (B-type, [ref]) and Ryugu (Cg-type, [ref]), while earlier work reported the Didymos system as an Xk-type (Binze et al. 2004)[3]. Sg-type asteroids consist of L/LL chondrite-like materials (Dunn et al. 2013). As ordinary chondrites usually have stronger mechanical strengths (e.g., Pohl & Britt 2020), if target materials are similar to such materials, the crater formation mechanism on Dimorphos is different from that on Bennu and Ryugu. In this case, a higher fraction of the impact kinetic energy may be used to fragment target materials during the impact process (e.g., Holsapple 1993; Wiggins et al. 2019), causing the crater formation to occur in the strength regime. If there exists high porosity, a large fraction of the energy may also be applied to reduce void space, which creates a smaller crater (Wünnemann et al. 2006; Collins et al. 2011). The near-surface properties are of importance for the size and morphology of the DART impact crater (i.e., Raducan et al. 2019; Raducan et al. 2020).

4.3. *Didymos reshaping scenarios*

This section summarizes the variations in reshaping (Figure 14). Sections 2.2.2 and 2.2.3 argue Didymos' structural sensitivity and its possible reshaping modes driven by fast rotation. The findings are that while rotational forces majorly contribute to the reshaping modes, they depend on the internal structure. The internal structure may be categorized into three types.

The first type is that Didymos consists of a mechanically weak, homogeneous structure but can still hold the body at the current spin period. This case may be analogous to Figure 4b. The structure starts deforming at a longer spin period. The central and surface regions both reach their yield conditions and experience inelastic deformation. The shape continuously deforms and eventually becomes a pancake-like shape. Materials at the edges finally depart from the body, and the body eventually disintegrates into streams of small particles. A body having a weaker interior and a stronger surface may deform similarly (Sánchez & Scheeres 2018).

The second type is made of a mechanically strong, homogeneous structure. This strong structure keeps the body from structural failure and thus can spin up at a shorter spin period. However, when the spin period reaches its critical limit, the body can no longer endure high stress, failing structurally. Unlike the first type, in which moving granular elements behave like more fluidized media, the body experiences significant fractures and falls apart into multiple pieces. This type may be similar to Figure 4c.

The third type represents a body having a weaker surface layer on top of a stronger interior. The surface layer first fails structurally at a longer spin period. As the spin period becomes shorter, surface materials move more actively towards the equatorial regions while the interior remains intact. However, the body falls apart when the structure can no longer remain intact due to the rotational force. Given a higher internal strength, because the critical spin period may be shorter, disintegrated elements experience higher rotational forces, leading to their immediate departure from the original body. A comparable process is given Figures 4d and 6. Also, active asteroid (6478) Gault's mass ejection at a relatively short spin period, ~2.5 h, suggesting that this asteroid's structure may be similar to this type (Jackson et al. 2021).

For the nominal DART impact scenario, the speed of the ejecta falling onto Didymos may be less than a few m/s because there are limited particles coming to get to Didymos straight (Yu et al. 2017; Yu & Michel 2018). Assuming that this case yields a potential reshaping process. The first type may be a weak structural configuration, which can possibly induce large deformation. Because of its weak structure, the necessary energy level to induce large deformation for this type may be lower than that for the other two types. Thus, even slow ejecta from the impact site hitting Didymos may disturb its sensitive surface, causing landslides and internal deformation. On the other hand, the second and third types may make a smaller reshaping process because the interior may resist such a process. For the third type, the surface areas may be more susceptible to landslides by slower ejecta falling, but the interior may still be structurally intact, keeping most of the shape configuration. Given the current structural conditions, the second and third types are likely, and the present study suggests that even small reshaping processes occurring to the second and third types may be high enough to induce measurable orbit perturbation.

---

[3] Some studies categorized Didymos as an Xk-type in their survey studies (e.g., de León et al. 2010; Carry et al. 2016).

Spin rate

a. Homogeneous structure (weak)

Internal structure

b. Homogeneous structure (strong)

c. Heterogenous structure (weakest on top and strongest inside)
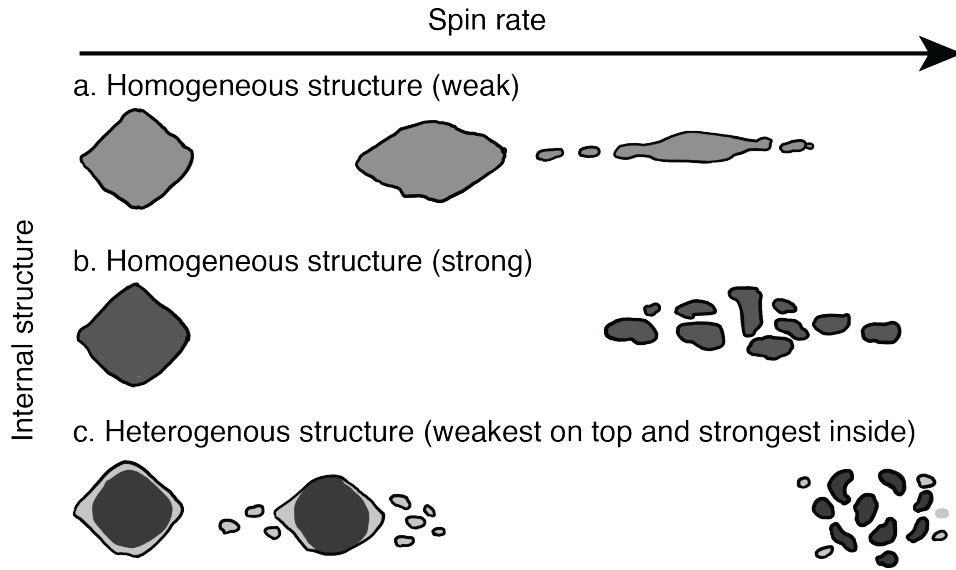
Figure 14 Potential reshaping mode depending different internal structure. The horizontal axis shows the spin rate. Going rightward gives a higher spin rate. a. Homogeneous weak structure. b. Homogeneous strong structure. c. Heterogeneous structure. The top layer in light gray consists of weaker structures, while the interior in dark gray is made of stronger structures.

4.4. *Occurrence of DART-driven reshaping depending on Didymos' surface condition*

At present, whether the DART-driven reshaping occurs on Didymos is not well constrained. The major reason is that it is not clear how Didymos' structure remains intact. If van der Waals force-based cohesion is the major contributor to the body's cohesive strength, smaller particles with sizes of $\sim 10\ \mu$ m must bridge and hold larger boulders. This condition implies the existence of small particles over the surface. On the other hand, if interlocking plays a key role in apparent strength, the structure only hosting large boulders can also hold the current shape. Depending on the structure that Didymos possesses, whether the DART-driven reshaping occurs may vary (Figure 15).

If Didymos' surface mainly consist of large boulders supported by interlocking (Figure 15a), a reshaping process is unlikely to occur by low-speed ejecta impacts. Such impacts do not affect the surface conditions because their kinetic energy is too low to create craters on boulders and move them, which are under the influence of higher contact forces (e.g., Tatsumi & Sugita 2018). If a surface layer consist of tiny particles, whether slow speed impact events induce a reshaping process depends on its mechanical strength (Figures 15b and 15c). A surface layer made of strongly bonded particles with a strength of higher than 25 Pa maintains its original condition without severe disturbance (Figures 15b). Subsequent slow-speed impacts are not efficient to break the mechanical bonds between particles, and the surrounding area does not experience any disturbance from the impacts. However, if low cohesive particles (less than 25 Pa) are dominant, localized disturbance may trigger a series of mass movements in larger regions (Figures 15c).

Further uncertainties include how the DART impact-driven ejecta approach Didymos. Ejecta dynamics simulations predict that if the DART impact is an ideal collision axisymmetrically generating its ejecta cone along the body's intermediate axis, the ejecta coming straight are unlikely to hit Didymos (Figure 16a). On the other hand, slow ejecta with a speed of $< 1\ \mathrm{m/s}$ may stay in the system, and some of them may fall onto it due to complex force fields. However, whether the nominal case is reasonable for the DART impact is uncertain. A limited capability presents measuring Dimorphos' geophysical properties, and thus the current analysis assumes this asteroid's shape to be a triaxial ellipsoid. Detailed telescopic observations reveal that irregular rubble pile asteroids are common (e.g., Benner et al. 2015). Thus, the triaxial ellipsoid assumption may make the present problem too ideal. In fact, Squannit, the secondary of Moshup, is not exactly a triaxial ellipsoid (Ostro et al. 2006). Also, Hayabusa2's SCI experiment exhibited its highly asymmetric ejecta cone, suggesting a strong dependence of ejecta generation on the surface condition (Arakawa et al. 2020). If Dimorphos is indeed different from the ideal condition, the ejecta cone geometry becomes complex as an impact on a sloping surface may change it (Figures 16b and 16c). If the ejecta cone faces inward and crosses Didymos, fast ejecta hit its surface, increasing the probability of a reshaping event. A variation in the surface slope up to 45° predicts leads

to a ~20% collision probability for ejecta faster than 14 m/s in speed and a ~10% collision probability for ejecta faster than 1 m/s in speed. Importantly, in addition to it, the spacecraft geometry (projectile shape) also changes the ejecta cone geometry (Raducan et al. 2022).

In sum, because of significant uncertainties of the physical properties, it is unclear whether this process occurs. Despite the lack of asserting what types of reshaping occur, such a process may not induce a collapse of Didymos' entire structure. The major reason is that if Didymos is extremely sensitive to a complete collapse and about to fail by low-speed impacts of the DART impact-driven ejecta, this body, which has experienced numerous impacts on multiple scales in the past, should not exist at present. On the contrary, a small-scale event is still possible and depends on how much ejecta hit Didymos' surface and cause a surface disturbance. In fact, this small-scale scenario is comparable to the top shape evolution under fast rotation over a long time scale (Cotto-Figueroa et al. 2015; Scheeres 2015; Scheeres et al. 2019, 2020). Therefore, exploring whether the DART-driven reshaping also reveals the history of top-shaped asteroids as well as the formation and evolution of binary asteroids [ref]. The Hera mission will provide key insights into such questions [ref].
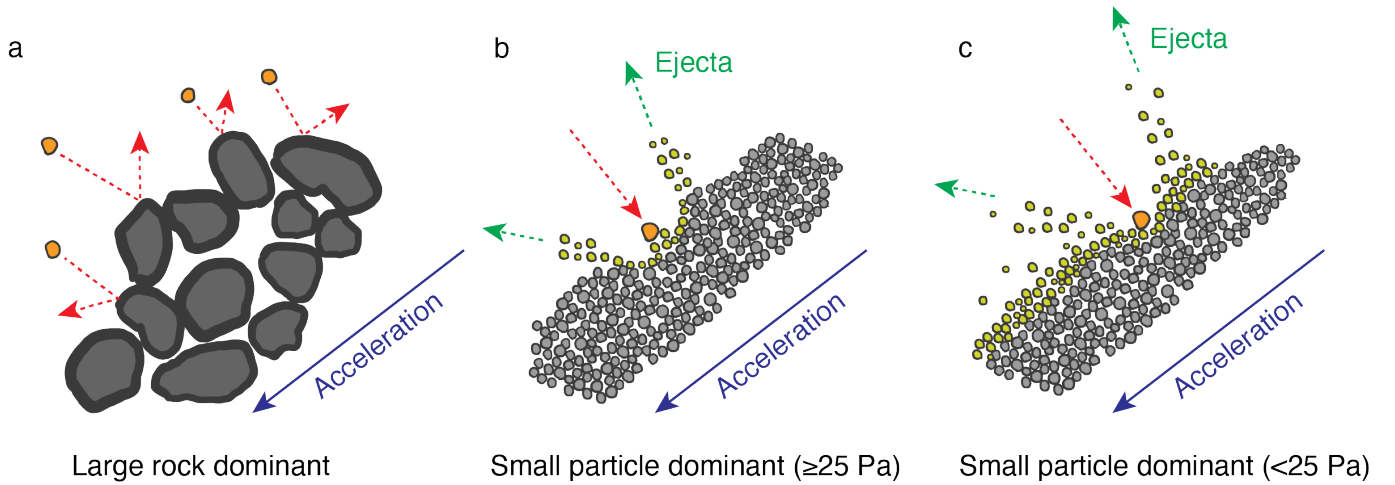
Figure 15 Low-speed particle collisions on Didymos under different surface conditions. a. Large rocks are dominant on the surface, and low-speed collisions do not affect the conditions. b. A surface layer with small, highly cohesive particles (≥ 25 Pa) is unaffected by low-speed collisions. c. Low-speed collisions on a small, low cohesive layer (< 25 Pa) may induce surface disturbance. Because the spin period of failure in this schematic is conceptual, it may change due to the existing strength.
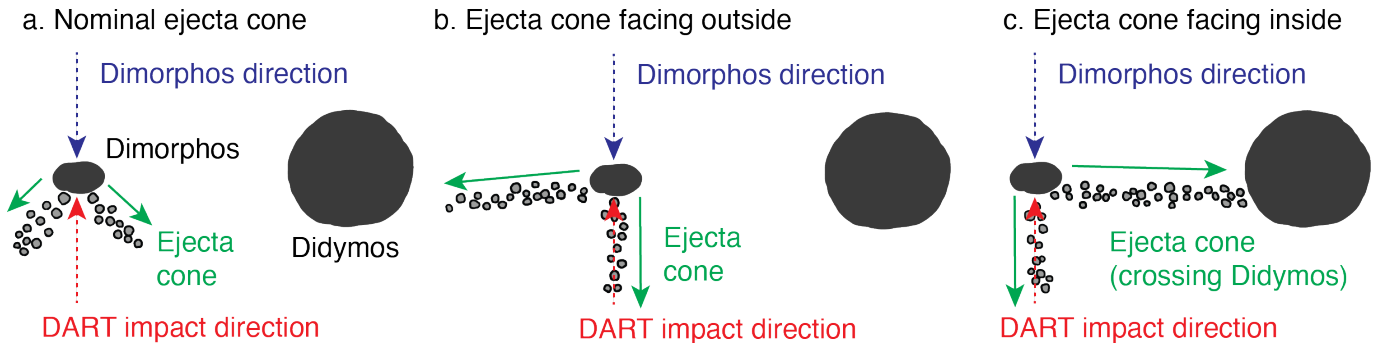
Figure 16 Variations in ejecta cone geometry driven by a sloping surface and the spacecraft shape. a. Nominal case generating axisymmetric cone geometry. b. Ejecta cone facing outward. c. Ejecta cone facing inward and eventually crossing Didymos.

5. CONCLUSION

This report discussed critical findings to interpret the dynamic and structural behaviors of the Didymos-Dimorphos system after the DART impact, which are listed below.

1. If Dimorphos consists of weak materials, and the DART impact occurs in the gravity regime, the impact process may be sub-catastrophic, changing the shape significantly. A gravity-regime impact may cause reshaping of 30 m along the impact direction on a 150 m diameter spherical body. This condition may be the end member of the impact process, inferring that the formation of a smaller crater is more likely on Dimorphos.

2. If the observed geophysical parameters are indeed true, Didymos' structure is close to its critical condition because of the 2.26 h spin period, which is near the spin limit. At this point, over the range of the bulk density, 1820 kg/m^3 to 2520 kg/m^3, the major part of the internal structure experiences a tensile stress and thus requires mechanical strength, such as cohesive strength and geologic interlocking, to support the current configuration.

3. If Didymos has the nominal bulk density, 2170 kg/m^3, the surface acceleration at the major part of the equator may depend on the rotational component, leading to higher surface slope distributions, which is consistent with earlier findings by Naidu et al. (2020). This result suggests that granular particles cannot stay on the surface unless they experience attractive forces to stick to it. If this is not the case, they depart from the surface, inferring the surface layer sensitivity. This acceleration field directly correlates with the internal stress field.

4. If some events trigger large deformation, the resulting reshaping process may be catastrophic. Given the structural condition, the deformation process may continue until it completely collapses. The reshaping mode strongly depends on the internal structure. A lower bulk density and a higher cohesive strength may cause a breakup into multiple large components, while a higher bulk density and a lower cohesive strength may induce surface-dominant activities. Furthermore, the existence of a mechanically strong core may also control the reshaping process. A large core with a limited surface layer can prevent a total collapse but enhance surface material movements.

5. If the surface structure has a cohesive strength of higher than 25 Pa, subsequent collisions of the DART-driven ejecta particles with an impact velocity of < 5 m/s do not disturb Didymos' surface layers at all. Thus, this case does not cause further reshaping processes, keeping the structure intact. However, a surface cohesive strength of less than 5 Pa, which may be a reasonable surface condition at middle and high latitudes, may yield subsequent mass movements.

6. Without the consideration of the influence of the spacecraft's complex geometry on the ejecta cone formation, the expected DART impact geometry relative to Didymos under a surface slope uncertainty of $< 45°$ gives a 20% chance of the DART-driven ejecta with a speed of $>\sim14$ m/s hitting Didymos and a 10% case of those with a speed of ~1 m/s encountering the asteroid.

7. If a reshaping process does occur on either Didymos or Dimorphos, the resulting gravitational variation causes orbital perturbation in the mutual system. If the magnitude of reshaping is large enough, Earth-based telescopes may detect reshaping-driven orbital perturbation. If there is reshaping larger than 2 m along the intermediate axis of Dimorphos, the orbital period change is higher than the DART measurement requirement, which is 7.3 s. For Didymos, a reshaping larger than 0.7 m along the short axis makes the orbital period change higher than the measurement requirement. Didymos' reshaping may be measurable by tracking its spin period change. Ligithcurve measurements may be capable of detecting reshaping of higher than 1 cm along the short axis.

The findings above describe the potential scenarios after the DART impact, though the key issue of this problem is large uncertainties of the system's physical properties. Thus, at present, it is challenging to predict what dynamic and structural responses actually happen after the DART impact. The scenarios strongly depend on Didymos' and Dimorphos' structural conditions, as well as how the DART driven ejecta particles arrive at Didymos and deliver kinetic energy to induce surface disturbance. Importantly, even if the DART impact does not cause any reshaping driven orbital perturbation, the outcomes are rich in constraining the internal structures of both these bodies. This problem is interdisciplinary, connecting multi physical processes, and the DART impact event offers a unique opportunity to quantify natural events happening to a binary system, which is one of the common asteroid classes in NEAs.

Table 2: Major physical parameters for the ejecta speed and cone geometry computation. The quantities represents the DART-impact conditions on Didymos. The crater scaling parameters are based on Richardson et al. (2007).

Notation	Description	Value	Units
g	Gravitational acceleration	4.975×10^{-5}	m/s^2
ρ_t	Target bulk density	2170	kg/m^3
R_g	Gravity-regime crater radius	45.71	m
R_s	Strength-regime crater radius ($C_0 = 2$ kPa)	14.76	m
C_{Tg}	Gravity-regime crater formation parameter	0.8	[-]
C_{Ts}	Strength-regime crater formation parameter	1.02	[-]
r	Distance from the impact point to the ejecta base	[-]	m
v_f	Ejection speed	[-]	m/s
ψ_f	Ejection angle	[-]	[-]
r	Distance from the impact point to the ejecta base	[-]	m
μ	Crater scaling parameter	0.41	[-]
ϵ	Stability parameter	1	Pa
ψ_0	Initial ejection angle	$52.4° \pm 6.1°$	[-]
ψ_d	Ejection angle variation	$18.4° \pm 8.2°$	[-]
ϕ_{im}	Impact angle	[-]	[-]
θ_{az}	Azimuth from the impactor incoming direction	[-]	[-]

6. ACKNOWLEDGMENTS

APPENDIX

A. EJECTION SPEED AND EJECTA CONE GEOMETRY

This appendix section briefly summarizes the scaling relationship approach that computes the ejection speed and angle (Richardson et al. 2007). The present model uses this approach to compute the ejection speed and angle at the DART impact site with a given surface slope, which is considered to be a statistical parameter. Table 2 lists the applied parameters. The calculation of the ejecta speed and angle starts by using the π-scaling relationship (Holsapple 1993) to calculate the crater radii in the gravity and strength regimes, R_g and R_s, respectively. We obtain these quantities as $R_g = 45.71$ m and $R_s = 14.76$ m.

These radii and the scaling parameters yield the crater formation timescales. When the crater formation is in the gravity regime, the crater formation timescale, T_g, is given as

$$T_g = C_{Tg}\sqrt{\frac{R_g}{g}} \tag{A1}$$

where C_{Tg} is the scaling parameter for the gravity regime and g is the gravitational acceleration for Dimorphos. On the other hand, the timescale in the strength regime, T_s, is given as

$$T_s = C_{Ts}R_s\sqrt{\frac{\rho_t}{C_0}} \tag{A2}$$

where C_{Ts} is the scaling parameter for the strength regime, ρ_t is the target bulk density, which is identical to ρ_B but nevertheless introduced for the following discussions, and C_0 is the cohesive strength. Richardson et al. (2007) introduced the effective strength $\bar{Y}$, instead of the cohesive strength C_0. Therefore, using C_0 may be inaccurate for general situations; in fact, Hirabayashi et al. (2020b) argued this is the case for larger bodies such as the Kuiper Belt

Object, Arrokoth. Because Dimorphos is small enough that the stress field is less than tens of Pa. Based on this, this study assumes that C_0 is comparable to $\bar{Y}$. These conditions yield $T_g = \sim 760$ s and $T_s = \sim 16$ s for $C_0 = 2$ kPa.

The model proceeds with determining the ejection speed and angle. Following Richardson et al. (2007) provides the ideal ejection speed without the effects of gravity and friction, v_e. For the gravity dominant regime, this quantity is given as

$$v_e(r) = C_{vpg} \sqrt{gR_g} \left(\frac{r}{R_g} \right)^{-\frac{1}{\mu}} \tag{A3}$$

where r is the distance from the impact point to the ejecta base on the target surface, and C_{vpg} is the scaling parameter, which is given as

$$C_{vpg} = \frac{\sqrt{2}}{C_{Tg}} \frac{\mu}{1+\mu} \tag{A4}$$

On the other hand, for the strength regime, it is given as

$$v_e(r) = C_{vps} \sqrt{\frac{C_0}{\rho_t}} \left(\frac{r}{R_s} \right)^{-\frac{1}{\mu}} \tag{A5}$$

where

$$C_{vps} = C_{vpg} \left(\frac{\rho_t g R_g}{C_0 + \epsilon} \right)^{\frac{1}{2}} \left(\frac{R_g}{R_s} \right)^{\frac{1}{\mu}} \tag{A6}$$

The ϵ parameter corresponds to the Y parameter in (Richardson et al. 2007), which is called the simulation stability parameter. Here, we fix it at 1 Pa. The v_e value does not account for a condition that the ejection speed is affected by gravity and friction. Applying the Bernoulli principle resolves this issue by constraining its value at the largest crater radius and obtains the ejection speed, v_{ef}:

$$v_{ef} = \sqrt{v_e^2 - C_{vpg}^2 gr - C_{vps}^2 \frac{C_0}{g}} \tag{A7}$$

The ejection angle, ψ_f, is formulated empirically (Richardson et al. 2007). First, the nominal ejecta angle, ψ_n, is computed as

$$\psi_n = \psi_0 - \psi_d \frac{r}{R_g} \tag{A8}$$

where ψ_0 is the initial ejecta angle, and ψ_d is the variation. If the impact event is oblique, the ejecta angle also depends on the impact angle, ϕ_{im}, and the azimum from the impact incoming direction, θ_{az}, which is given as

$$\psi_f = \psi_n - \frac{\pi \cos\phi_{im}(1 - \cos\theta_{az})}{12} \left(1 - \frac{r}{R_g} \right)^2 \tag{A9}$$

$\phi_{im} = 90°$ is the normal impact. Using the ejection angle finally determines the actual ejection speed:

$$v_f = v_{ef} \sin\psi_n \sqrt{1 + \cot^2\psi_f} \tag{A10}$$

There are two caveats of this approach. First, Equation (A7) uses the ejection speed without the influence of gravity and friction under the assumption that the ejection angle is 45°. This comes from the computation of C_{vpg} in Equation (A4); in this equation, the $\sqrt{2}$ terms result from the assumption of the normal ejection angle being 45°, i.e., $\sin(45°) = \sqrt{2}$. However, the ejection angle is later set to vary to compute v_f. Thus, a proper calculation of the ejection angle may need an implicit solver to simultaneously determine v_f and ϕ_f. This process may rather be complex. This study uses the same approach as Richardson et al. (2007). Second, this scaling relationship approach assumes a flat target surface, while the DART impact on Dimorphos is likely not this case. The shape irregularity

680 may change the ejection speed and ejecta cone geometry. However, numerous uncertainties of the geophysical and
681 impact conditions prevent further analysis. This study, therefore, focuses on providing rough estimates of the ejecta
682 conditions. Importantly, as shown in Figure 9, fast ejecta may give a higher probability of collision events. For this
683 case, the ejection timescale is quite short after the DART impact, and the surface may reasonably be assumed to be
684 flat, meaning that the derived probability for this case is meaningful. On the other hand, the slow ejecta cases may
685 need revision because they are likely affected by complex local topographies.

REFERENCES

Agrusa, H. F., Gkolias, I., Tsiganis, K., et al. 2021, Icarus, 370, doi: 10.1016/j.icarus.2021.114624

Annex, A. M., Pearson, B., Seignovert, B., et al. 2020, Journal of Open Source Software, 5, 2050, doi: 10.21105/joss.02050

Arakawa, M., Saiki, T., Wada, K., et al. 2020, Science, 368, 67, doi: 10.1126/science.aaz1701

Barnouin, O. S., Daly, M. G., Palmer, E. E., et al. 2019, Nature Geoscience, 12, 247, doi: 10.1038/s41561-019-0330-x

Becker, T. M., Howell, E. S., Nolan, M. C., et al. 2015, Icarus, 248, 499, doi: 10.1016/j.icarus.2014.10.048

Benner, L. A. M., Busch, M. W., Giorgini, J. D., et al. 2015, in Asteroids IV (Tucson: Univ. of Arizona), 165–182, doi: 10.2458/azu_uapress_9780816532131-ch009

Binze, R. P., et al. 2004, Icarus, 170, 259, doi: 10.1016/j.icarus.2004.04.004

Carry, B., et al. 2016, Icarus, 238, 340, doi: 10.1016/j.icarus.2015.12.047

Cheng, A. F., Michel, P., Jutzi, M., et al. 2016, Planetary and Space Science, 121, 27, doi: 10.1016/j.pss.2015.12.004

Cheng, A. F., Rivkin, A. S., Michel, P., et al. 2018, The Planetary and Space Science, 157, 104

Cheng, A. F., et al. 2020, Icarus, 352, doi: 10.1016/j.icarus.2020.113989

Collins, G. S., Melosh, H. J., & Ivanov, B. A. 2004, Meteoritics & Planetary Science, 39, 217, doi: 10.1111/j.1945-5100.2004.tb00337.x

Collins, G. S., Melosh, H. J., & Wünnemann, K. 2011, International Journal of Impact Engineering, 38, 434, doi: 10.1016/j.ijimpeng.2010.10.013

Cotto-Figueroa, D., Statler, T. S., Richardson, D. C., et al. 2015, The Astrophysical Journal, 803, 25

Daly, R. T., Bierhaus, E. B., Barnouin, O. S., et al. 2020, Geophysical Research Letters, 47, e2020GL089672, doi: 10.1029/2020GL089672

de León, J., et al. 2006, Advances in Space Research, 37, 178, doi: 10.1016/j.asr.2005.05.074Get

—. 2010, Astronomy & Astrophysics, 517, A23, doi: 10.1051/0004-6361/200913852

Dunn, T. L., et al. 2013, Icarus, 222, 273, doi: 10.1016/j.icarus.2012.11.007

et al., F. 2022a, Planetary Science Journal

et al., S. 2022b, Planetary Science Journal

Ferrari, F., Lavagna, M., & Blazquez, E. 2020, Monthly Notices of the Royal Astronomical Society, 492, 749, doi: 10.1093/mnras/stz3458

Ferrari, F., & Tanga, P. 2022, (submitted)

Ferrari, F., Tasora, A., Masarati, P., & Lavagna, M. 2017, Multibody System Dynamics, 39, 3, doi: 10.1007/s11044-016-9547-2

Harris, A. W., et al. 2009, Icarus, 199, 310

Hergenrother, C. W., Maleszewski, C. K., Nolan, M. C., et al. 2019, Nature Communications, 10, doi: 10.1038/s41467-019-09213-x

Hirabayashi, M. 2015, Monthly Notices of the Royal Astronomical Society, 454, 2249–2257, doi: 10.1093/mnras/stv2017

Hirabayashi, M., Davis, A. B., Fahnestock, E. G., et al. 2019a, Advances in Space Research, 63, 2515, doi: 10.1016/j.asr.2018.12.041

Hirabayashi, M., Nakano, R., Tatsumi, E., et al. 2020a, Icarus, 352, 113946, doi: 10.1016/j.icarus.2020.113946

Hirabayashi, M., Sánchez, D. P., & Scheeres, D. J. 2015, The Astrophysical Journal, 808, 63, doi: 10.1088/0004-637X/808/1/63

Hirabayashi, M., Tatsumi, E., Miyamoto, H., et al. 2019b, The Astrophysical Journal Letters, 874, L10, doi: 10.3847/2041-8213/ab0e8b

Hirabayashi, M., Trowbridge, A. J., & Bodewits, D. 2020b, The Astrophysical Journal Letters, 891, doi: 10.3847/2041-8213/ab3e74

Hirabayashi, M., et al. 2017, Monthly Notices of the Royal Astronomical Society, 472, 1641

Hirata, N., & Ikeya, R. 2021, Icarus, 364, 114474, doi: 10.1016/j.icarus.2021.114474

Holsapple, K. A. 1993, Annu. Rev. Earth Planet. Sci., 21, doi: 10.1146/annurev.ea.21.050193.002001

Holsapple, K. A., & Housen, K. R. 2012, Icarus, 221, 875, doi: 10.1016/j.icarus.2012.09.022

Housen, K. R., Sweet, W. J., & Holsapple, K. A. 2018, Icarus, 300, 72, doi: 10.1016/j.icarus.2017.08.019

Jackson, P. M., Nakano, R., Kim, Y., et al. 2021, ArXiv, arXiv:2112.11582, accepted in PSJ

Jacobson, S. A., Marzari, F., Rossi, A., & Scheeres, D. J. 2016, Icarus, 277, 381, doi: 10.1016/j.icarus.2016.05.032

Jacobson, S. A., & Scheeres, D. J. 2011, Icarus, 214, 161, doi: 10.1016/j.icarus.2011.04.009

Jawin, E. R., Walsh, K. J., Barnouin, O. S., et al. 2020, JGR:Planets, 125, e2020JE006475, doi: 10.1029/2020JE006475

Jutzi, M. 2015, Planet. Space Sci, 107, 3, doi: 10.1016/j.pss.2014.09.012

—. 2019, Planetary and Space Science, 177, 104695, doi: 10.1016/j.pss.2019.07.009

Jutzi, M., Benz, W., & Michel, P. 2008, Icarus, 198, 242, doi: 10.1016/j.icarus.2008.06.013

Lambe, T. W., & Whitman, R. V. 1969, Soil Mechanics (John Wiley & Sons)

Lauretta, D. S., Hergenrother, C. W., Chesley, S. R., et al. 2019, Science, 366, doi: 10.1126/science.aay3544

Margot, J.-L., Pravec, P., Taylor, P., et al. 2015, in Asteroids IV (Tucson: Univ. of Arizona), 355–374, doi: 10.2458/azu_uapress_9780816532131-ch019

Meyer, A. J., Gkolias, I., Gaitanas, M., et al. 2021, The Planetary Science Journal, 2, 224, doi: 10.3847/PSJ/ac3b1

Michel, P., Ballouz, R.-L., Barnouin, O. S., et al. 2020, Nature Communications, 11, doi: 10.1038/s41467-020-16433-z

Murrary, C. D., & Dermott, S. F. 2000, Solar System Dynamics (Cambridge University Press)

Naidu, S., Benner, L., Brozovic, M., et al. 2020, Icarus, 113777, doi: 10.1016/j.icarus.2020.113777

Naidu, S. P., Margot, J.-L., Taylor, P. A., et al. 2015, The Astronomical Journal, 150, 54, doi: 10.1088/0004-6256/150/2/54

Nakano, R., & Hirabayashi, M. 2022, Planetary Science Journal, Submitted to PSJ

Nolan, M. C., Howell, E. S., Scheeres, D. J., et al. 2019, Geophysical Journal Letters, 46, 1956, doi: 10.1029/2018GL080658

Ostro, S. J., et al. 2006, Science, 314, 1276

Pohl, L., & Britt, D. T. 2020, Meteoritics & Planetary Science, 55, 962, doi: 10.1111/maps.13449

Pravec, P., Harris, A., & Warner, B. 2008, Proceedings of the International Astronomical Union, 2, 167, doi: 10.1017/S1743921307003201

Pravec, P., Scheirich, P., Kušniráka, P., et al. 2006, Icarus, 181, 63, doi: 10.1016/j.icarus.2005.10.014

Raducan, S. D., Davison, T. M., & Collins, G. S. 2020, Planetary and Space Science, 104756, doi: 10.1016/j.pss.2019.104756

Raducan, S. D., Davison, T. M., Luther, R., & Collins, G. S. 2019, Icarus, 329, 282, doi: 10.1016/j.icarus.2019.03.040

Raducan, S. D., & Jutzi, M. 2022, Planetary Science Journal

Raducan, S. D., Jutzi, M., Davison, T. M., et al. 2022, International Journal of Impact Engineering

Rainey, E. S. G., Stickle, A. M., Cheng, A. F., et al. 2020, International Journal of Impact Engineering, 142, 103528, doi: 10.1016/j.ijimpeng.2020.103528

Richardson, D. C., Agrusa, H. F., Barbee, B. W., et al. 2022, The Planetary Science Journal, Submitted

Richardson, D. C., Leinhardt, Z. M., Melosh, H. J., & Michel, P. 2002, in Asteroids III, ed. W. F. Bottke, A. Cellino, P. Paolicchi, & P. R. Binzel (Tucson: Univ. of Arizona), 501–515

Richardson, J. E., Melosh, H. J., Lisse, C. M., et al. 2007, Icarus, 191, 176, doi: 10.1016/j.icarus.2007.08.033

Rivkin, A. S., et al. 2021, Planetary Science Journal, Accepted

Roberts, J., Barnouin, O., Daly, M., et al. 2021, Planetary and Space Science, 204, 105268, doi: 10.1016/j.pss.2021.105268

Sánchez, P., & Scheeres, D. J. 2014, Meteoritics & Planetary Science, 49, 788, doi: 10.1111/maps.12293

Sánchez, P., & Scheeres, D. J. 2018, Planetary and Space Science, 157, 39, doi: 10.1016/j.pss.2018.04.001

Sánchez Lana, D. P., & Scheeres, D. J. 2018, in American Astronomical Society, DPS meeting 50, id.312.14

Scheeres, D., Hartzell, C., Sánchez, P., & Swift, M. 2010, Icarus, 210, 968, doi: 10.1016/j.icarus.2010.07.009

Scheeres, D. J. 2015, Icarus, 247, 1, doi: 10.1016/j.icarus.2014.09.017

Scheeres, D. J., McMahon, J. W., French, A. S., et al. 2019, Nature Astronomy, 3, 352, doi: 10.1038/s41550-019-0721-3

Scheeres, D. J., French, A. S., Tricarico, P., et al. 2020, Science Advances, 6, eabc3350, doi: 10.1126/sciadv.abc3350

Schwartz, S. R., Richardson, D. C., & Michel, P. 2012, Granular Matter, 14, 363, doi: https://doi.org/10.1007/s10035-012-0346-z

Soldini, S., Takanao, S., Ikeda, H., et al. 2020, Planetary and Space Science, 180, 104740, doi: https://doi.org/10.1016/j.pss.2019.104740

Stickle, A. M., Bruck Syal, M., Cheng, A. F., et al. 2020, Icarus, 338, 113446, doi: 10.1016/j.icarus.2019.113446

Stickle, A. M., Rainey, E. S. G., Bruck Syal, M., et al. 2017,
    Procedia Engineering, 204, 116,
    doi: 0.1016/j.proeng.2017.09.763

Tatsumi, E., & Sugita, S. 2018, Icarus, 300, 227,
    doi: 10.1016/j.icarus.2017.09.004

Taylor, P. A., Howell, E. S., Nolan, M. C., et al. 2012, in
    AAS, AAS Meeting 220, id.128.02

Walsh, K. J., Jawin, E. R., Ballouz, R.-L., et al. 2019,
    Nature Geoscience, 12, 242,
    doi: 10.1038/s41561-019-0326-6

Walsh, K. J., et al. 2006, Nature, 454, 188

Walsh, W. J., & Jacobson, S. A. 2015, in Asteroids IV
    (Tucson: Univ. of Arizona), 375–393,
    doi: 10.2458/azu_uapress_9780816532131-ch020

Watanabe, S., et al. 2019, Science, 364, 268

Wiggins, S. E., Johnson, B. C., Bowling, T. J., et al. 2019,
    Journal of Geophysical Research: Planets, 124, 941,
    doi: 10.1029/2018JE005757

Wünnemann, K., Collins, G. S., & Melosh, H. J. 2006,
    Icarus, 180, 514, doi: 10.1016/j.icarus.2005.10.013

Yu, Y., Cheng, B., Hayabayashi, M., Michel, P., & Baoyin,
    H. 2019, Celestial Mechanics and Dynamical Astronomy,
    131, 1

Yu, Y., & Michel, P. 2018, Icarus, 312, 128 ,
    doi: https://doi.org/10.1016/j.icarus.2018.04.017

Yu, Y., Michel, P., Hirabayashi, M., et al. 2018, The
    Astronomical Journal, 156,
    doi: 10.3847/1538-3881/aaccf7

Yu, Y., Michel, P., Schwartz, S. R., Naidu, S. P., & Benner,
    L. A. 2017, Icarus, 282, 313,
    doi: https://doi.org/10.1016/j.icarus.2016.09.008

Zhang, Y., Michel, P., Richardson, D. C., et al. 2021,
    Icarus, 362, 114433,
    doi: https://doi.org/10.1016/j.icarus.2021.114433

Zhang, Y., Richardson, D. C., Barnouin, O. S., et al. 2017,
    Icarus, 294, 98,
    doi: https://doi.org/10.1016/j.icarus.2017.04.027